Dynamic Rupture and Earthquake Sequence Simulations Using the Wave Equation in Second-Order Form

Kenneth Duru[a, e], Kali L. Allison[b,c], Maxime Rivet[d], and Eric M. Dunham[b,d]

[a]Department of Earth and Environmental Sciences, Munich University, Munich, Germany
[b]Department of Geophysics, Stanford University, Stanford, California, USA
[c]present affiliation: Department of Geology, University of Maryland, College Park, Maryland, USA
[d]Institute for Computational and Mathematical Engineering, Stanford University, Stanford, California, USA
[e]present affiliation: Mathematical Sciences Institute, Australian National University, Canberra, Australia

June 10, 2019

Abstract

We present a numerical method for simulating both single-event dynamic ruptures and earthquake sequences with full inertial effects in antiplane shear with rate-and-state fault friction. We use the second-order form of the wave equation, expressed in terms of displacements, discretized with high-order-accurate finite difference operators in space. Advantages of this method over other methods include reduced computational memory usage and reduced spurious high frequency oscillations. Our method handles complex geometries, such as nonplanar fault interfaces and free surface topography. Boundary conditions are imposed weakly using penalties. We prove time stability by constructing discrete energy estimates. We present numerical experiments demonstrating the stability and convergence of the method, and showcasing applications of the method, including the transition in rupture style from crack-like ruptures to slip pulses for strongly rate-weakening friction and the simulation of earthquake sequences in a viscoelastic solid with a fully dynamic coseismic phase.

keywords: Friction, Seismic cycle, Wave propagation, Numerical modelling, Numerical approximations and analysis, Earthquake dynamics

1 Introduction

Computer simulations of earthquake rupture propagation and event sequences are now widely used to understand controls on rupture behavior, ground motion, and how interactions between aseismic slip and off-fault viscous flow at depth load the seismogenic zone to create earthquakes. Traditionally, earthquake simulations have focused on single rupture events, accounting for inertial effects like seismic waves but often starting from ad hoc or idealized initial conditions with artificial initiation procedures (e.g., Day, 1982; Dunham et al., 2011; Kozdon et al., 2012; Shi and Day, 2013; Douilly et al., 2015; Andrews and Ma, 2016). Simulations have also focused on sequences of earthquakes, accounting for aseismic slip and nucleation but neglecting or approximating inertia during the coseismic phase (e.g., Rice, 1993; Ben-Zion and Rice, 1995; Kato, 2002; Ziv and Cochard, 2006; Segall and Bradley, 2012; Erickson and Dunham, 2014; Allison and Dunham, 2018). Only a few simulation methods combine event sequence modeling with fully dynamic ruptures (e.g. Lapusta et al., 2000; Lapusta and Liu, 2009; Noda and Lapusta, 2010; Barbot et al., 2012).

The computational challenge with fully dynamic sequence simulations is finding a method that provides relatively seamless transitions between the coseismic phase, where inertia is important, and other phases, in which the material response is effectively quasi-static. The numerical method should ideally be written in a way that inertia can be disabled by eliminating the density times acceleration term in the momentum balance. Not all methods have this property. For example, the first-order form of the wave equation (i.e., written as a first-order hyperbolic system of equations) is widely used for wave propagation studies (e.g., Marfurt, 1984; Virieux, 1986; Saenger et al., 2000; Zingg, 2000; Kozdon et al., 2012), partly due to the maturity of numerical methods for first-order systems. This formulation utilizes the time derivative of Hooke's law, rather than Hooke's law directly, and therefore the quasi-static limit of the governing equations is still time dependent. In contrast, inertia can be eliminated from the second-order form of the wave equation (i.e., written in terms of displacements) to yield the static elasticity equation.

Both finite difference and finite element methods can be used to solve the second-order form of the wave equation. For finite difference methods, there are additional benefits to the use of the second-order form. It reduces spurious high frequency oscillations which can occur when using standard central difference schemes for first-order systems on unstaggered grids (these oscillations are greatly reduced on staggered grids). Relative to the first-order unstaggered formulation, the second-order formulation also requires fewer grid points to achieve the same accuracy, and requires less computational memory. For a more thorough discussion of the advantages of second-order form, see Kreiss et al. (2002).

Finite differences are typically limited to second-order accuracy due to difficulties in selecting the difference stencil near boundaries and enforcing boundary conditions. These difficulties are particularly challenging for earthquake modeling, where the fault interface conditions involve nonlinear relations between tractions and discontinuities in displacement or particle velocities. In this work, we utilize specially designed difference operators and boundary/interface condition enforcement known, respectively, as summation-by-parts (SBP) operators Mattsson (2011) and the simultaneous approximation term (SAT) penalty method. With SBP-SAT, the generalization to high-order accuracy, even near boundaries and interfaces, is straightforward (Duru et al., 2014; Duru and Virta, 2014). High-order-accurate

SBP-SAT finite difference methods have been applied to earthquake modeling, but thus far only in the context of the first-order velocity-stress formulation of the wave equation (Kozdon et al., 2012, 2013) or the static elasticity problem (Allison and Dunham, 2018; Erickson and Day, 2016). Here we extend this approach to the second-order form of the wave equation.

We use a high-order-accurate SBP finite difference scheme for the wave equation. High-order finite difference methods are well-suited for wave propagation problems, in part because they can be designed to produce a diagonal mass matrix, and because of their low dispersion errors (Kreiss and Oliger, 1972). The advantage of SBP methods is that the discretization can be designed to mimic the energy balance of the continuous problem, producing a discretization that can be proven to be strictly stable (Duru et al., 2014; Duru and Virta, 2014). This allows the discretization scheme to be used for systems that do not allow growth in time, a feature which is important for earthquake simulations, especially in the context of earthquake sequences, which require the simulation to be run over a long time frame.

The second-order form of elastic wave equation in curvilinear coordinates is presented in Appelö and Petersson (2009) with second-order accuracy, and extended to fourth-order accuracy in Sjögreen and Petersson (2011). Methods for handling a variety of boundary conditions, including traction and Dirichlet conditions, and internal interfaces, are presented in Duru et al. (2014) and Duru and Virta (2014). The primary contribution of this paper is to develop the scheme for friction laws, which are interface conditions with nonlinear dependence on the slip velocity, history of sliding, and tractions acting on the fault.

In the rest of this paper, we first describe the governing equations for the continuous problem and derive the energy balance equation. We then develop the discretization and prove stability. Finally, we present numerical experiments verifying the accuracy and convergence of the method and demonstrating some of its capabilities.

2 Continuous Analysis

In this section, we present and analyze the continuous model in Cartesian and curvilinear coordinates. We derive the energy balance for friction laws, encapsulated in the rate-and-state framework, in prestressed elastic solids. We end this section by discussing and prescribing necessary and sufficient conditions required for the well-posedness of state evolution laws.

2.1 Cartesian Coordinates

Consider the antiplane shear problem with the displacement field $\mathbf{u} = (0, 0, u)$ and $\partial u/\partial z \equiv 0$, where ρ, μ are the density and shear modulus. Let the spatial domain consist of two elastic blocks $\Omega = \Omega_- \cup \Omega_+$ separated by a fault at $x = \widetilde{x}\,(y)$, that is

$$\Omega_- = (-\infty, \widetilde{x}] \times (-\infty, \infty) \quad \text{and} \quad \Omega_+ = [\widetilde{x}, \infty) \times (-\infty, \infty)\,. \tag{1}$$

This is illustrated in Figure 1, and corresponds to strike-slip fault which extends infinitely along strike. The fault is defined by the arbitrarily oriented smooth curve $x = \widetilde{x}\,(y)$ separating the two elastic media. If the fault is planar then we consider $\widetilde{x} = x_0$, where x_0 is a real constant. Fields and material properties on the positive side of the fault, $x > \widetilde{x}$, are denoted with a superscript $+$, (u^+, μ^+, ρ^+), and on the negative side of the fault, $x < \widetilde{x}$, denoted with a superscript $-$, (u^-, μ^-, ρ^-). The shear wave speed is $c^\pm = \sqrt{\mu^\pm/\rho^\pm}$.

We consider linear elastic deformations about an equilibrium, prestressed reference configuration. The initial stress tensor is

$$\bar{\bar{\sigma}}^0 = \begin{pmatrix} \sigma^0_{xx} & \sigma^0_{xy} & \sigma^0_{xz} \\ \sigma^0_{xy} & \sigma^0_{yy} & \sigma^0_{yz} \\ \sigma^0_{xz} & \sigma^0_{yz} & \sigma^0_{zz} \end{pmatrix}.$$

With the direction of slip parallel to the z-axis, the momentum balance equation in each half-space is

$$\rho \frac{\partial^2 u}{\partial t^2} = \frac{\partial \sigma_{xz}}{\partial x} + \frac{\partial \sigma_{yz}}{\partial y}, \tag{2}$$

with Hooke's law

$$\sigma_{xz} = \sigma^0_{xz} + \mu \frac{\partial u}{\partial x}, \quad \sigma_{yz} = \sigma^0_{yz} + \mu \frac{\partial u}{\partial y}. \tag{3}$$

The above equations are combined to obtain the scalar wave equation with a time invariant source term,

$$\rho \frac{\partial^2 u}{\partial t^2} = \frac{\partial}{\partial x}\left(\mu \frac{\partial u}{\partial x}\right) + \frac{\partial}{\partial y}\left(\mu \frac{\partial u}{\partial y}\right) + F(x,y). \tag{4}$$

where

$$F(x,y) = \frac{\partial \sigma^0_{xz}}{\partial x} + \frac{\partial \sigma^0_{yz}}{\partial y} \equiv 0,$$

the latter equality following from equilibrium of the prestressed reference state. On the fault, the tractions $T^\pm = T^\pm_0 + \Delta T^\pm$, slip $[\![u]\!]$, and slip velocity V are defined by

$$\Delta T^\pm := \mp \mu^\pm \frac{\partial u^\pm}{\partial n^\pm}, \quad [\![u]\!] := u^+ - u^-, \quad V := \frac{\partial [\![u]\!]}{\partial t}, \quad x = \widetilde{x}, \tag{5}$$

where $T^\pm_0$ are the background tractions (i.e., prestress resolved on the fault, as explained in more detail in the next section) and $\Delta T^\pm$ are the evolving changes in fault tractions associated with the displacement field. Here, $\partial/\partial n^\pm$ is the normal derivative on the fault, and $n = n^- = -n^+$, having $T^-_0 = -T^+_0 = T_0$. On a planar fault, $x = x_0$, we have $n = (1,0)^T$ and the normal derivative is $\partial/\partial n = \partial/\partial x$.

2.2 Curvilinear Coordinates and Transformation

For nonplanar fault geometries it is necessary to transform the equation of motion Eq. (4) to a coordinate system $[q,r] \in [0,1]^2$ so that numerical treatments can be performed efficiently. We define the transformation by $(x(q,r), y(q,r)) \leftrightarrow (q(x,y), r(x,y))$, such that the new coordinates form a regular Cartesian grid. We choose our coordinate transformations such that the fault is located at $q = 0$. See Figure 1 for a schematic description.

The transformed equation of motion is

$$\widehat{\rho} \frac{\partial u}{\partial t^2} = \frac{\partial}{\partial q}\left(\widehat{A} \frac{\partial u}{\partial q} + \widehat{C} \frac{\partial u}{\partial r}\right) + \frac{\partial}{\partial r}\left(\widehat{B} \frac{\partial u}{\partial r} + \widehat{C}\ \frac{\partial u}{\partial q}\right) + \widehat{F}(q,r). \tag{6}$$

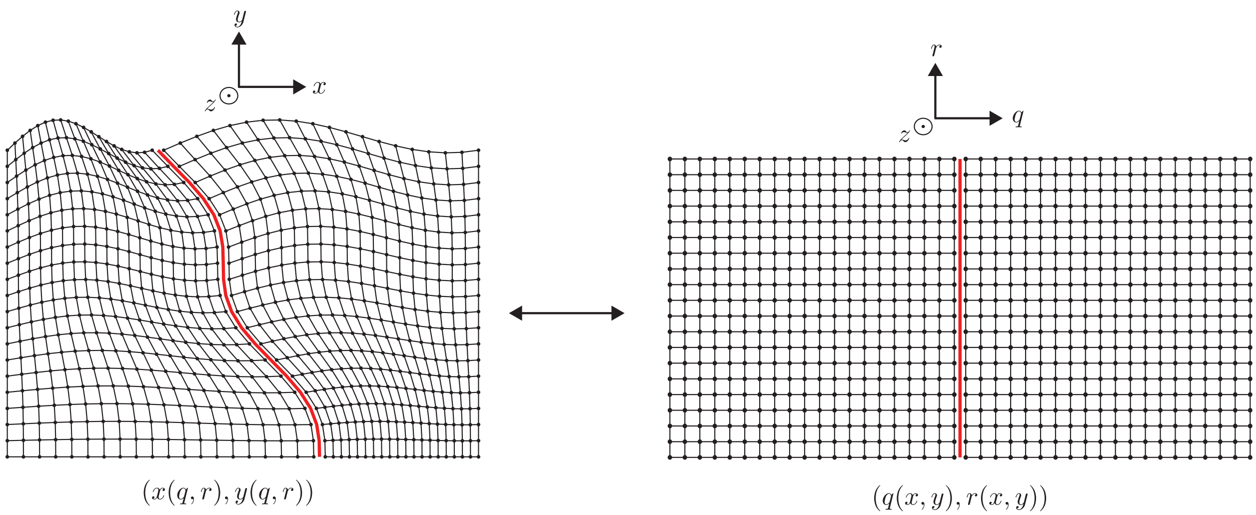

Figure 1: Diagram of the domain in curvilinear coordinates (left) and on a regular Cartesian grid (right). The fault is shown in red.

where

$$\widehat{F}(q,r) = JF(x,y) = \frac{\partial}{\partial q}\left(J(q_x\sigma^0_{xz} + q_y\sigma^0_{yz})\right) + \frac{\partial}{\partial r}\left(J(r_x\sigma^0_{xz} + r_y\sigma^0_{yz})\right) \equiv 0.$$

The Jacobian of the transformation is $J = x_q y_r - x_r y_q > 0$, and the metric relations are

$$Jq_x = y_r, \quad Jq_y = -x_r, \quad Jr_x = -y_q, \quad Jr_y = x_q. \tag{7}$$

Here, the subscripts denote partial metric derivatives, that is $x_q = \partial x/\partial q$, $q_x = \partial q/\partial x$, etc. The transformed variable material properties are

$$\widehat{\rho} = J\rho, \quad \widehat{A} = J\left(q_x^2 + q_y^2\right)\mu, \quad \widehat{B} = J\left(r_x^2 + r_y^2\right)\mu, \quad \widehat{C} = J\left(q_x r_x + q_y r_y\right)\mu. \tag{8}$$

Since the fault is at $q = 0$, the normal vector to the fault, pointing into the positive block Ω_+, is

$$n = \frac{1}{\sqrt{q_x^2 + q_y^2}}\begin{pmatrix} q_x \\ q_y \end{pmatrix}, \tag{9}$$

and the resolved background shear traction and traction change on the fault take the form

$$T_0 = n_x\sigma^0_{xz} + n_y\sigma^0_{yz}, \quad \Delta T = \frac{1}{J\sqrt{q_x^2 + q_y^2}}\left(\widehat{A}\frac{\partial u}{\partial q} + \widehat{C}\frac{\partial u}{\partial r}\right). \tag{10}$$

Thus, we have

$$T = T_0 + \Delta T = \frac{1}{J\sqrt{q_x^2 + q_y^2}}\left(J\sqrt{q_x^2 + q_y^2}T_0 + \left(\widehat{A}\frac{\partial u}{\partial q} + \widehat{C}\frac{\partial u}{\partial r}\right)\right).$$

We will now formulate the frictional interface conditions coupling the two elastic solids on the fault.

2.3 Energy Balance with Friction

The interface conditions are force balance and the friction law

$$\Delta T^- = -\Delta T^+ = \Delta T, \quad T := \quad T_0 + \Delta T = \sigma_0 \frac{f\left(|V|, \psi\right)}{|V|} V, \tag{11}$$

with $f\left(0, \psi\right) = 0$ and $\partial f\left(V, \psi\right)/\partial V > 0$. Here, $\sigma_0 > 0$ is the compressive normal stress, T_0 is the initial shear traction resolved on the fault, $f\left(|V|, \psi\right)$ is the friction coefficient, V is the slip-rate, and ψ is the state variable. Note that

$$V \to 0 \iff \sigma_0 \frac{f\left(|V|, \psi\right)}{|V|} \to \infty. \tag{12}$$

Throughout this study, we consider formulations in which the state variable ψ is non-dimensional and is governed by the generic state evolution equation

$$\frac{d\psi}{dt} = g\left(|V|, \psi\right). \tag{13}$$

Note that Eq. (13) is an ordinary differential equation (ODE) for state ψ. In general $f\left(|V|, \psi\right)$ and $g\left(|V|, \psi\right)$ are empirical expressions obtained from laboratory experiments (Dieterich, 1979; Rice and Ruina, 1983; Ruina, 1983). The friction law is constructed such that energy is dissipated on the fault.

To be precise, let the transformed strain energy matrix P be denoted by

$$P = S^T \mu S, \quad S = \begin{pmatrix} q_x & r_x \\ q_y & r_y \end{pmatrix}. \tag{14}$$

Since μ is real and positive, it follows from (14) that P is symmetric positive definite, with

$$\begin{pmatrix} \frac{\partial u}{\partial q} \\ \frac{\partial u}{\partial r} \end{pmatrix}^T P \begin{pmatrix} \frac{\partial u}{\partial q} \\ \frac{\partial u}{\partial r} \end{pmatrix} = \mu \left(q_x \frac{\partial u}{\partial q} + r_x \frac{\partial u}{\partial r} \right)^2 + \left(q_y \frac{\partial u}{\partial q} + r_y \frac{\partial u}{\partial r} \right)^2 = \mu \left(\left(\frac{\partial u}{\partial x} \right)^2 + \left(\frac{\partial u}{\partial y} \right)^2 \right). \tag{15}$$

Now, introduce the kinetic energy density

$$K = \frac{\rho}{2} \left(\frac{\partial u}{\partial t} \right)^2 > 0, \tag{16}$$

and the strain energy density

$$U = U_0 + \frac{1}{2} \begin{pmatrix} \frac{\partial u}{\partial q} \\ \frac{\partial u}{\partial r} \end{pmatrix}^T P \begin{pmatrix} \frac{\partial u}{\partial q} \\ \frac{\partial u}{\partial r} \end{pmatrix} + \begin{pmatrix} \frac{\partial u}{\partial q} \\ \frac{\partial u}{\partial r} \end{pmatrix}^T S^T \begin{pmatrix} \sigma_{xz}^0 \\ \sigma_{yz}^0 \end{pmatrix}, \tag{17}$$

where U_0 is an arbitrary reference energy and the next two terms represent the work, per unit volume, done against the stress changes and the prestress, respectively, by deformation of the solid. The above definition coincides with standard expressions in mechanics (Kostrov, 1974; Rudnicki and Freund, 1981).

It is desirable for the analysis to follow that U, or at least the portion of U for which $dU/dt \neq 0$, be of quadratic form. For numerical analysis, the quadratic form can be used to define (discrete) energy-norms, so that numerical stability and convergence can be easily proven. To this end, we make the specific choice of $U_0 = [(\sigma_{yz}^0)^2 + (\sigma_{xz}^0)^2]/(2\mu)$, and it follows that

$$
\begin{aligned}
U &= \frac{1}{2}\begin{pmatrix} \frac{\partial u}{\partial q} \\ \frac{\partial u}{\partial r} \end{pmatrix}^T P \begin{pmatrix} \frac{\partial u}{\partial q} \\ \frac{\partial u}{\partial r} \end{pmatrix} + \begin{pmatrix} \frac{\partial u}{\partial q} \\ \frac{\partial u}{\partial r} \end{pmatrix}^T S^T \begin{pmatrix} \sigma_{xz}^0 \\ \sigma_{yz}^0 \end{pmatrix} + \frac{1}{2\mu}\left(\left(\sigma_{yz}^0\right)^2 + \left(\sigma_{xz}^0\right)^2\right) \\
&= \frac{\mu}{2}\left(\left(\frac{\partial u}{\partial x}\right)^2 + \left(\frac{\partial u}{\partial y}\right)^2\right) + \sigma_{xz}^0 \frac{\partial u}{\partial x} + \sigma_{yz}^0 \frac{\partial u}{\partial y} + \frac{1}{2\mu}\left(\left(\sigma_{xz}^0\right)^2 + \left(\sigma_{yz}^0\right)^2\right) \qquad (18) \\
&= \frac{1}{2\mu}\left(\left(\mu\frac{\partial u}{\partial x} + \sigma_{xz}^0\right)^2 + \left(\mu\frac{\partial u}{\partial y} + \sigma_{yz}^0\right)^2\right) > 0.
\end{aligned}
$$

The elastic energy is defined by

$$
\mathrm{E} = \int_0^1 \int_0^1 (K + U)\, J dq dr > 0. \qquad (19)
$$

Theorem 1. *Consider the wave equation Eq.* (6) *with the interface condition Eq.* (11). *Let* E^+ *denote the elastic energy of the positive block* Ω^+ *and* E^- *denote the elastic energy of the negative block* Ω^-. *The sum of the elastic energies satisfies*

$$
\frac{d}{dt}\left(\mathrm{E}^-(t) + \mathrm{E}^+(t)\right) = -\int_0^1 \sigma_0 |V| f\left(|V|, \psi\right) \left(J\sqrt{q_x^2 + q_y^2}\right)_{q=0} dr, \quad \forall \psi, \qquad (20)
$$

Proof. We use the energy method, that is, we multiply Eq. (6) with $\partial u/\partial t$, add the transpose of the product and integrate over the whole domain. Integration by parts, and considering boundary contributions from the fault only (while ignoring other boundaries) gives

$$
\frac{d\mathrm{E}^-(t)}{dt} = \int_0^1 \frac{\partial u^-}{\partial t} T \left(J\sqrt{q_x^2 + q_y^2}\right)_{q=0} dr, \quad \frac{d\mathrm{E}^+(t)}{dt} = -\int_0^1 \frac{\partial u^+}{\partial t} T \left(J\sqrt{q_x^2 + q_y^2}\right)_{q=0} dr, \qquad (21)
$$

where we have utilized the fact that $\partial U_0/\partial t \equiv 0$ and $\widehat{F}^{\pm}(q, r) \equiv 0$. Adding the contribution from both sides of the fault and enforcing the interface condition Eq. (11) completes the proof. □

Noting that $\left(J\sqrt{q_x^2 + q_y^2}\right)_{q=0} dr$ is the arclength along the fault, the above energy balance states that energy in the solid is dissipated during frictional sliding on the fault.

If the slip-rate vanishes, $V = 0$, then the right-hand side of the energy rate in Eq. (20) also vanishes: $d\left(\mathrm{E}^-(t) + \mathrm{E}^+(t)\right)/dt = 0$. When, $V \neq 0$, and $f\left(|V|, \psi\right) > 0$, then the elastic energy is dissipated.

Note that in Eq. (20), if $f(|V|, \psi) \geq 0$ then the elastic energy is dissipated for all ψ, but, the energy equation Eq. (20) does not provide any bound on ψ. Therefore, in order for the energy equation Eq. (20) to be well defined the state evolution equation Eq. (13) must have precisely one solution for each $V \in \mathbb{R}$ and initial condition. Next, we will prescribe necessary and sufficient conditions required for the well-posedness of the state evolution law Eq. (13). This will be useful in designing a convergent high-order-accurate scheme.

2.4 Admissible State Evolution Laws

Natural earthquakes arise from frictional instabilities during sliding along fault surfaces. Therefore, state evolution equations modeling an earthquake must allow for physically unstable solutions. However, in order for the model to be useful it must be well-posed.

In Eq. (20), if $f(|V|, \psi) \geq 0$ then the slip-rate V is bounded for all ψ. Consider now the state evolution equation Eq. (13). The function $g\left(|V|, \psi\right)$ is Lipschitz continuous in ψ, if $|g\left(|V|, \psi_1\right) - g\left(|V|, \psi_2\right)| \leq L|\psi_1 - \psi_2|$ with the Lipschitz constant $L > 0$. If $g\left(|V|, \psi\right)$ is differentiable then $L = \max_{\xi} |\partial g(|V|, \xi)/\partial \xi|$ is a Lipschitz constant.

We will now state a fundamental result which can be found in standard textbooks on ordinary differential equations, see for instance Birkhoff and Rota (1989) and Dahlquist (2010).

Theorem 2. *If $g\left(|V|, \psi\right)$ satisfies a Lipschitz condition in the whole of $\mathbb{R}$ then the initial value problem Eq.* (13) *has precisely one solution for each $V \in \mathbb{R}$ and initial condition. The solution has a continuous first time derivative for all t.*

If the Lipschitz condition holds in a subset $\mathbb{D}$ of $\mathbb{R}$ only, then existence and uniqueness hold as long as the orbit stays in $\mathbb{D}$.

A typical rate-and-state friction coefficient is (Rice et al., 2001)

$$f(|V|, \psi) = a \operatorname{arcsinh}\left(\frac{|V|}{2V_0} e^{\psi/a}\right), \tag{22}$$

where the friction parameters a and V_0 are real and positive. These parameters will be described below. Note that $f(|V|, \psi) \geq 0$, for all ψ. Common evolution laws for the state variable ψ are (Ruina, 1983; Marone, 1998)

1. Aging law:
$$g(|V|, \psi) = \frac{bV_0}{d_c}\left(e^{(f_0-\psi)/b} - \frac{|V|}{V_0}\right), \tag{23}$$

2. Slip law:
$$g(|V|, \psi) = -\frac{|V|}{d_c}\left(f(|V|, \psi) - f_{ss}(|V|)\right), \tag{24}$$

where $f_{ss}(V)$ is an arbitrary steady state friction coefficient. Some commonly used forms of the steady state friction coefficient are the standard expression (e.g. Rice et al., 2001)

$$f_{ss}(|V|) = f_0 - (b-a)\ln\frac{|V|}{V_0}, \tag{25}$$

and the strongly rate-weakening friction law (Dunham et al., 2011)

$$f_{ss}(|V|) = f_w + \frac{f_{LV} - f_w}{\left(1 + (|V|/V_w)^n\right)^{1/n}}, \quad f_{LV}(V) = f_0 - (b-a)\ln\frac{|V|}{V_0}. \tag{26}$$

Here, a is the direct effect parameter, b is evolution effect parameter, V_0 is the reference slip velocity, d_c is the state-evolution distance, f_0 is the steady state friction coefficient at V_0,

V_w is the weakening slip-rate, f_w is the fully weakened friction coefficient, and $n > 0$ is a positive real number.

For the strongly rate-weakening friction law, we have $f_{ss} \approx f_{LV}$ if $|V| \ll V_w$ and $f_{ss} \approx f_w$ if $|V| \gg V_w$. The parameter n controls the abruptness of the transition between the two limits. In the limit $n \to \infty$, the original flash-heating model (Rice, 1999; Beeler and Tullis, 2003; Rice, 2006; Beeler et al., 2008) emerges. The onset of strongly rate-weakening behavior can be kept smooth by choosing finite values of n. As in Dunham et al. (2011), to have a smooth transition, we choose $n = 8$. This is necessary for ensuring accurate numerical treatments.

The state evolution laws Eq. (23)–(24) are differentiable with

$$\text{Aging law:} \quad \frac{\partial g(|V|,\psi)}{\partial \psi} = -\frac{V_0}{d_c} e^{(f_0-\psi)/b} < 0, \tag{27}$$

$$\text{Slip law:} \quad \frac{\partial g(|V|,\psi)}{\partial \psi} = -\frac{|V|^2}{2V_0 d_c} \frac{e^{\psi/a}}{\sqrt{1 + \frac{e^{2\psi/a}}{4V_0^2}|V|^2}} < 0, \tag{28}$$

for all ψ. We remark that the aging law and the slip law are differentiable, and hence satisfy the admissible conditions for state evolution laws. Note also that a steady state solution ψ_{ss}, satisfying $g\left(|V|, \psi_{ss}\right) = 0$, is a local attractor in the context of dynamical systems (Birkhoff and Rota, 1989). This implies that any sufficiently small perturbation $\psi(t) = \psi_{ss} + \delta\psi(t)$ around the steady state ψ_{ss}, will asymptotically converge to the steady state, $\delta\psi(t) \to 0$ and $\psi(t) \to \psi_{ss}$, as $t \to \infty$.

3 Semi-Discrete Approximations and Analysis

Next, we discretize the continuous problem in space. To begin, consider the discretization of the unit interval $r \in [0,1]$ into N_r grid points with a uniform spatial step $h > 0$

$$r_j = (j-1)h, \quad j = 1,\dots,N_r, \quad h = 1/(N_r - 1). \tag{29}$$

Introduce the one-dimensional finite difference operators $D_r \approx \partial/\partial r$ and $D_{rr}^{(\widehat{B})} \approx \partial/\partial r\left(\widehat{B}\partial/\partial r\right)$, the finite difference approximations of the first and second derivatives in the unit interval Eq. (29). We will use fully compatible SBP finite operators (Duru and Virta, 2014) to approximate all spatial derivatives. Therefore, the finite difference operators D_r, $D_{rr}^{(\widehat{B})}$ satisfy the following properties:

$$D_r = H^{-1}Q, \quad Q + Q^T = E_R + E_L, \quad \mathbf{v}^T H \mathbf{v} > 0, \tag{30}$$

$$D_{rr}^{(\widehat{B})} = H^{-1}(-M^{(\widehat{B})} + (E_R + E_L)\widehat{B} D_r), \quad M^{(\widehat{B})} = \left(M^{(\widehat{B})}\right)^T, \quad \mathbf{v}^T M^{(\widehat{B})} \mathbf{v} \ge 0, \tag{31}$$

$$M^{(\widehat{B})} = D_r^T H \widehat{B} D_r + R^{(\widehat{B})}, \quad R^{(\widehat{B})} = \left(R^{(\widehat{B})}\right)^T, \quad \mathbf{v}^T R^{(\widehat{B})} \mathbf{v} \ge 0. \tag{32}$$

Here, the matrices $E_R = \operatorname{diag}(0,0,\dots,0,1)$ and $E_L = \operatorname{diag}(-1,0,\dots,0,0)$ pick out the right and left boundary terms. The matrix Q is almost skew-symmetric and H is diagonal with $H_{jj} = h_j^{(r)} = \gamma_j h$, $\gamma_j > 0$ where $h > 0$ is the uniform spatial step defined in Eq. (29). In Eq. (32) above, the higher order term $R^{(\widehat{B})}$ is called the remainder operator. We use narrow stencil approximations for $D_{rr}^{(\widehat{B})}$, with $R^{(\widehat{B})} \neq 0$, as opposed to wide stencil approximations; see also Mattsson (2011). If $D_{rr}^{(\widehat{B})}$ is constructed by applying D_r twice, we will have $R^{(\widehat{B})} \equiv 0$, and the operator would correspond to a wide stencil approximation. Wide stencil approximations allow spurious high frequency (π-mode) oscillations. The narrow stencil approximation, with $R^{(\widehat{B})} \neq 0$, can eliminate the spurious π-mode oscillations without destroying the accuracy of $D_{rr}^{(\widehat{B})}$. See Duru and Virta (2014) and Duru et al. (2014) for more details on SBP finite difference operators for second derivatives.

3.1 Semi-Discrete Approximation

We discretize the transformed equation of motion (6) using the SBP operators, defined in Eq. (30)–(31), and impose the boundary conditions using penalties. To begin, discretize the unit square with the uniform spatial steps

$$\begin{aligned} q_i &= (i-1)h_q, \quad i = 1, \ldots, N_q, \quad h_q = 1/(N_q - 1), \\ r_j &= (j-1)h_r, \quad j = 1, \ldots, N_r, \quad h_r = 1/(N_r - 1). \end{aligned}$$

The two-dimensional semi-discrete solution is stacked, row-wise, as a vector of length $N_q N_r$. The 2D spatial operators are $\mathbf{D}_q \approx \partial/\partial q$, $\mathbf{D}_r \approx \partial/\partial r$, $\mathbf{D}_{qq}^{(\widehat{A})} \approx \partial/\partial q \left(\widehat{A}\partial/\partial q\right)$, and $\mathbf{D}_{rr}^{(\widehat{B})} \approx \partial/\partial r \left(\widehat{B}\partial/\partial r\right)$. They can be written in a more compact form using Kronecker products with the identity matrices, I_q, I_r, and the 1D spatial finite difference operators D_r, D_q defined in Eq. (30) such that

$$\begin{aligned} &\mathbf{D}_r = I_q \otimes D_r, \quad \mathbf{D}_q = D_q \otimes I_r, \quad \mathbf{H}_r = I_q \otimes H_r, \quad \mathbf{H}_q = H_q \otimes I_r, \quad \mathbf{H} = \mathbf{H}_q \otimes \mathbf{H}_r, \\ &\mathbf{E}_{Rr} = I_q \otimes E_R, \quad \mathbf{E}_{Lr} = I_q \otimes E_L, \quad \mathbf{E}_{Rq} = E_R \otimes I_r, \quad \mathbf{E}_{Lq} = E_L \otimes I_r, \\ &\mathbf{D}_{qq}^{(\widehat{A})} = \mathbf{H}_q^{-1}\left(-\mathbf{M}_q^{(\widehat{A})} + (\mathbf{E}_{Rq} + \mathbf{E}_{Lq})\widehat{A}\mathbf{D}_q\right), \quad \mathbf{D}_{rr}^{(\widehat{B})} = \mathbf{H}_r^{-1}\left(-\mathbf{M}_r^{(\widehat{B})} + (\mathbf{E}_{Rr} + \mathbf{E}_{Lr})\widehat{B}\mathbf{D}_r\right). \end{aligned}$$

The matrices $\widehat{A}$, $\widehat{B}$, $\widehat{C}$, denoting the transformed coefficients, are diagonal Eq. (8). Using these operators and introducing $|\mathbf{q}| = \sqrt{\mathbf{q}_x^2 + \mathbf{q}_y^2}$, the semi-discrete approximation of the equation of motion Eq. (6) with weak enforcement of the fault/interface condition Eq. (11) is

$$\begin{aligned} \widehat{\rho}^{-}\frac{\mathrm{d}^2\mathbf{u}^-}{\mathrm{d}t^2} &= \widehat{\mathcal{D}}^{\mu^-}\mathbf{u}^- + \widehat{\mathbf{F}}^- - \mathbf{H}_q^{-1}\mathbf{E}_{Rq}\mathbf{J}|\mathbf{q}|\left(\mathbf{T}_0 - \boldsymbol{\sigma}_0\frac{f\left(|\mathbf{V}|, \boldsymbol{\psi}\right)}{|\mathbf{V}|}\mathbf{V}\right), \\ \widehat{\rho}^{+}\frac{\mathrm{d}^2\mathbf{u}^+}{\mathrm{d}t^2} &= \widehat{\mathcal{D}}^{\mu^+}\mathbf{u}^+ + \widehat{\mathbf{F}}^+ - \mathbf{H}_q^{-1}\mathbf{E}_{Lq}\mathbf{J}|\mathbf{q}|\left(\mathbf{T}_0 - \boldsymbol{\sigma}_0\frac{f\left(|\mathbf{V}|, \boldsymbol{\psi}\right)}{|\mathbf{V}|}\mathbf{V}\right), \end{aligned} \tag{33}$$

$$\frac{d\boldsymbol{\psi}}{dt} = g(|\mathbf{V}|, \boldsymbol{\psi}), \tag{34}$$

with

$$\mathbf{V} = \left(V_1, V_2, \cdots, V_{N_r}\right)^T, \quad \boldsymbol{\psi} = \left(\psi_1, \psi_2, \cdots, \psi_{N_r}\right)^T,$$

defined at every grid point on the fault. Here,

$$\widehat{\mathcal{D}}^{\mu^{\pm}} = \mathbf{D}_{qq}^{(\widehat{A})} + \mathbf{D}_{rr}^{(\widehat{B})} + \mathbf{D}_q \widehat{C} \mathbf{D}_r + \mathbf{D}_r \, \widehat{C} \, \mathbf{D}_q - \mathbf{H}_q^{-1} \mathbf{E}_{\pm} \left(\widehat{A} \mathbf{D}_q + \widehat{C} \mathbf{D}_r \right), \quad \mathbf{E}_{-} = \mathbf{E}_{Rq}, \quad \mathbf{E}_{+} = \mathbf{E}_{Lq}, \tag{35}$$

and

$$\widehat{\mathbf{F}}^{\pm} = \mathbf{D}_q \left(\mathbf{J} (\mathbf{q}_x \boldsymbol{\sigma}_{xz}^0 + \mathbf{q}_y \boldsymbol{\sigma}_{yz}^0) \right) + \mathbf{D}_r \left(\mathbf{J} (\mathbf{r}_x \boldsymbol{\sigma}_{xz}^0 + \mathbf{r}_y \boldsymbol{\sigma}_{yz}^0) \right) \approx 0. \tag{36}$$

The nonlinear friction law appears in the semi-discrete approximation Eq. (33) as nonlinear source terms on the fault.

We have explicitly appended the approximated time invariant source term, $\widehat{\mathbf{F}}$, to the semi-discrete problem Eq. (33). The source term $\widehat{\mathbf{F}}$ will be zero if the background shear stress is zero. The source term can also vanish if the background shear stress is spatially uniform and the metric relations Eq. (7) are satisfied exactly by their discrete counterparts. However, in a general mesh, the source term $\widehat{\mathbf{F}}$ is proportional to the truncation error, and will only vanish in the limit of mesh refinement, if the numerical approximation is consistent.

It is also possible to omit the source term $\widehat{\mathbf{F}}$ in Eq. (33). This will not affect accuracy, since $\widehat{\mathbf{F}}$ is independent of the solution, but depends on the truncation error of finite difference operators, and it vanishes in the limit of mesh refinement. However, as we will see below, the omission of the source term $\widehat{\mathbf{F}}$ in Eq. (33) will have a slight impact on the stability of the semi-discrete approximation Eq. (33).

3.2 Semi-Discrete Stability

We will now establish the stability of the semi-discrete approximation Eq. (33). To begin, we introduce

$$\mathcal{A} = (\mathbf{H}_q \otimes \mathbf{H}_r) \, \widehat{\mathcal{D}}^{\mu} = \left(\mathbf{H}_r \mathbf{M}_q^{(\widehat{A})} + \mathbf{H}_q \mathbf{M}_r^{(\widehat{B})} + \mathbf{D}_q^T \mathbf{H} \widehat{C} \mathbf{D}_r + \mathbf{D}_r^T \mathbf{H} \, \widehat{C} \, \mathbf{D}_q \right). \tag{37}$$

Note that $\mathcal{A} = \mathcal{A}^T$ and

$$\begin{aligned}
\frac{1}{2} \mathbf{u}^T \mathcal{A} \mathbf{u} &= \frac{1}{2} \begin{pmatrix} \mathbf{D}_q \mathbf{u} \\ \mathbf{D}_r \mathbf{u} \end{pmatrix}^T \begin{pmatrix} \mathbf{HJ} & \mathbf{0} \\ \mathbf{0} & \mathbf{HJ} \end{pmatrix} P \begin{pmatrix} \mathbf{D}_q \mathbf{u} \\ \mathbf{D}_r \mathbf{u} \end{pmatrix} + \frac{1}{2} \mathbf{u}^T \mathbf{H}_r R_q^{(\widehat{A})} \mathbf{u} + \frac{1}{2} \mathbf{u}^T \mathbf{H}_q R_r^{(\widehat{B})} \mathbf{u} \\
&= \sum_{i=1}^{N_q} \sum_{j=1}^{N_r} \frac{\boldsymbol{\mu}_{ij}}{2} \left(\left((\mathbf{q}_{xij} \mathbf{D}_q \mathbf{u})_{ij} + \mathbf{r}_{xij} \left(\mathbf{D}_r \mathbf{u} \right)_{ij} \right)^2 + \left((\mathbf{q}_{xij} \mathbf{D}_q \mathbf{u})_{ij} + \mathbf{r}_{xij} \left(\mathbf{D}_r \mathbf{u} \right)_{ij} \right)^2 \right) \mathbf{J}_{ij} h_i^{(q)} h_j^{(r)} \\
&+ \frac{1}{2} \mathbf{u}^T \mathbf{H}_r R_q^{(\widehat{A})} \mathbf{u} + \frac{1}{2} \mathbf{u}^T \mathbf{H}_q R_r^{(\widehat{B})} \mathbf{u} > 0.
\end{aligned} \tag{38}$$

The matrix $\mathcal{A}$ is symmetric and positive definite. We introduce the semi-discrete kinetic and strain energies

$$\mathbf{K}(t) = \frac{1}{2} \frac{d\mathbf{u}}{dt}^T \left(\widehat{\rho} \mathbf{H} \right) \frac{d\mathbf{u}}{dt} > 0,$$

$$\mathbf{U}(t) = \frac{1}{2}\mathbf{u}^T \mathcal{A}\mathbf{u} + \begin{pmatrix} \mathbf{D}_q\mathbf{u} \\ \mathbf{D}_r\mathbf{u} \end{pmatrix}^T \mathbf{S}^T \begin{pmatrix} \mathbf{HJ} & \mathbf{0} \\ \mathbf{0} & \mathbf{HJ} \end{pmatrix} \begin{pmatrix} \boldsymbol{\sigma}^0_{xz} \\ \boldsymbol{\sigma}^0_{yz} \end{pmatrix} + \mathbf{U}_0,$$

where

$$\mathbf{U}_0 = \sum_{i=1}^{N_q}\sum_{j=1}^{N_r} \frac{1}{2\boldsymbol{\mu}_{ij}} \left(|\boldsymbol{\sigma}^0_{xzij}|^2 + |\boldsymbol{\sigma}^0_{yzij}|^2\right) \mathbf{J}_{ij} h_i^{(q)} h_j^{(r)}. \tag{39}$$

Note that

$$\begin{aligned}
\mathbf{U}(t) = &\sum_{i=1}^{N_q}\sum_{j=1}^{N_r} \left(\left(\frac{1}{2\boldsymbol{\mu}_{ij}} \left(\boldsymbol{\mu}_{ij} \left(\mathbf{q}_{xij} \left(\mathbf{D}_q\mathbf{u}\right)_{ij} + \mathbf{r}_{xij} \left(\mathbf{D}_r\mathbf{u}\right)_{ij} \right) + \boldsymbol{\sigma}^0_{xz} \right)^2 \right) \right) \mathbf{J}_{ij} h_i^{(q)} h_j^{(r)} \\
&+ \sum_{i=1}^{N_q}\sum_{j=1}^{N_r} \left(\left(\frac{1}{2\boldsymbol{\mu}_{ij}} \left(\boldsymbol{\mu}_{ij} \left(\mathbf{q}_{yij} \left(\mathbf{D}_q\mathbf{u}\right)_{ij} + \mathbf{r}_{yij} \left(\mathbf{D}_r\mathbf{u}\right)_{ij} \right) + \boldsymbol{\sigma}^0_{yz} \right)^2 \right) \right) \mathbf{J}_{ij} h_i^{(q)} h_j^{(r)} \\
&+ \frac{1}{2}\mathbf{u}^T \mathbf{H}_r R_q^{(\widehat{A})}\mathbf{u} + \frac{1}{2}\mathbf{u}^T \mathbf{H}_q R_r^{(\widehat{B})}\mathbf{u} > 0.
\end{aligned}$$

Define the semi-discrete quantity

$$\mathcal{E}\left(t\right) := \mathbf{K}(t) + \mathbf{U}(t), \tag{40}$$

where the first term on the right-hand side approximates the kinetic energy and the second term approximates the strain energy. The semi-discrete quantity $\mathcal{E}\left(t\right)$ defined in Eq. (40) is strictly positive, thus defining a semi-discrete energy.

We have

Theorem 3. *Consider the semi-discrete approximation Eq.* (33)*. The sum of the semi-discrete energies on both sides of the fault satisfies*

$$\frac{d}{dt}\left(\mathcal{E}^-\left(t\right) + \mathcal{E}^+\left(t\right)\right) = -\sum_{j=1}^{N_r} \sigma_0 |V_j(t)| f\left(|V_j(t)|, \psi_j\left(t\right)\right) J_{Nj} |\boldsymbol{q}_{Nj}| h_j^{(r)}. \tag{41}$$

Proof. We use the discrete energy method, that is, from the left we multiply the first and second equations in Eq. (33) with $\left(d\mathbf{u}^-/dt\right)^T \mathbf{H}$ and $\left(d\mathbf{u}^+/dt\right)^T \mathbf{H}$, respectively, add the transpose of the product. Using the summation-by-parts properties Eqs. (30)–(32), and considering boundary contributions from the fault only (while ignoring other boundaries) gives

$$\frac{d}{dt}\mathcal{E}^-\left(t\right) = \sum_{j=1}^{N_r} \frac{du^-_{Nj}(t)}{dt} \widehat{T}_j(t) J_{Nj} |\mathbf{q}_{Nj}| h_j^{(r)}, \quad \frac{d}{dt}\mathcal{E}^+\left(t\right) = -\sum_{j=1}^{N_r} \frac{du^+_{1j}(t)}{dt} \widehat{T}_j(t) J_{Nj} |\mathbf{q}_{Nj}| h_j^{(r)} \tag{42}$$

with

$$\widehat{T}_j(t) = \sigma_{0j} \frac{f\left(|V_j|, \psi_j\right)}{|V_j|} V_j,$$

where we have utilized the fact that $d\mathbf{U}_0/dt \equiv 0$. Adding the contributions from both sides of the fault completes the proof. □

The semi-discrete energy estimate Eq. (41) is analogous to the continuous estimate Eq. (20) in Theorem 1. The semi-discrete energy is dissipated by friction, $[\mathcal{E}^-(t) + \mathcal{E}^+(t)] \le [\mathcal{E}^-(0) + \mathcal{E}^+(0)]$, for all $t \ge 0$. However, for physically realistic models (Rice, 1983; Scholz, 1998) the derivative of the nonlinear friction coefficient can be extremely large, $\max|\partial f(V,\psi)/\partial V| \to \infty$, preventing the use of standard explicit time-stepping schemes such as Runge-Kutta methods to advance Eq. (33) in time. It is noteworthy that for the velocity-stress formulation, it is possible to circumvent this stiffness difficulty by introducing transformed variables, encoding the friction law on the fault (Kozdon et al., 2012). However, the construction of these transformed variables require the solution of a nonlinear algebraic problem.

Remark 1. *If we had omitted the vanishing source term $\widehat{\mathbf{F}}$ in Eq. (33), we would have the energy equation*

$$\begin{aligned} \frac{d}{dt}\left(\mathcal{E}^-(t) + \mathcal{E}^+(t)\right) = &-\sum_{j=1}^{N_r} \sigma_0 |V_j(t)| f\left(|V_j(t)|, \psi_j(t)\right) J_{Nj} |\boldsymbol{q}_{Nj}| h_j^{(r)} \\ &- \sum_{i=1}^{N_q}\sum_{j=1}^{N_r}\left(\frac{d\mathbf{u}_{ij}^-}{dt}\widehat{\mathbf{F}}_{ij}^- + \frac{d\mathbf{u}_{ij}^+}{dt}\widehat{\mathbf{F}}_{ij}^+\right) h_i^{(q)} h_j^{(r)}, \end{aligned} \tag{43}$$

and

$$\sqrt{[\mathcal{E}^-(t) + \mathcal{E}^+(t)]} \le \sqrt{[\mathcal{E}^-(0) + \mathcal{E}^+(0)]} + \sqrt{\left[\left(\widehat{\mathbf{F}}^-\right)^T (\widehat{\rho}^-\mathbf{H})\,\widehat{\mathbf{F}}^- + \left(\widehat{\mathbf{F}}^+\right)^T (\widehat{\rho}^+\mathbf{H})\,\widehat{\mathbf{F}}^+\right]}\, t.$$

The scheme is accurate and stable, but, there is a linear growth in energy. However, the growing term is proportional to the truncation error and will vanish in the limit of mesh refinement.

4 Fully-Discrete Approximation and Analysis

Here, we present the fully discrete numerical approximation. We will begin by discretizing the time variable $t \ge 0$, then approximate the time derivatives in Eq. (33) by second-order-accurate finite differences. We will formulate an iterative procedure for solving the nonlinear frictional algebraic problem on the fault. We conclude this section by proving stability of the fully discrete approximation.

4.1 Time Discretization

Discretize the time variable t with a uniform time step, $t_n = n\Delta t$, with $n = 0, 1, \ldots$. To derive an efficient and stable fully discrete numerical approximation we replace the time derivatives in Eq. (33) with second-order-accurate centered finite difference approximations, yielding

$$\widehat{\rho}^- \frac{\mathbf{u}_{n+1}^- - 2\mathbf{u}_n^- + \mathbf{u}_{n-1}^-}{\Delta t^2} = \widehat{\mathcal{D}}^{(\mu^-)}\mathbf{u}_n^- + \widehat{\mathbf{F}}^- - \mathbf{H}_q^{-1}\mathbf{E}_{Rq}\mathbf{J}|\mathbf{q}|\left(\mathbf{T}_0 - \sigma_0 \frac{f\left(|\mathbf{V}_n|, \psi_n\right)}{|\mathbf{V}_n|}\mathbf{V}_n\right), \tag{44}$$

$$\widehat{\rho}^+ \frac{\mathbf{u}_{n+1}^+ - 2\mathbf{u}_n^+ + \mathbf{u}_{n-1}^+}{\Delta t^2} = \widehat{\mathcal{D}}^{(\mu^+)}\mathbf{u}_n^+ + \widehat{\mathbf{F}}^+ - \mathbf{H}_q^{-1}\mathbf{E}_{Lq}\mathbf{J}|\mathbf{q}|\left(\mathbf{T}_0 - \sigma_0 \frac{f\left(|\mathbf{V}_n|, \psi_n\right)}{|\mathbf{V}_n|}\mathbf{V}_n\right), \tag{45}$$

where

$$\mathbf{V}_n = \frac{[\![\mathbf{u}]\!]_{n+1} - [\![\mathbf{u}]\!]_{n-1}}{2\Delta t}. \tag{46}$$

We will evolve Eq. (34) in time with a time-stepping scheme, such that the evolution of the state variable will not limit further the explicit time-step. The semi-discrete state evolution equation (34) is discretized in time using the implicit leap-frog scheme, we have

$$\frac{\boldsymbol{\psi}_{n+1} - \boldsymbol{\psi}_{n-1}}{2\Delta t} = g\left(|\mathbf{V}_n|, \frac{\boldsymbol{\psi}_{n+1} + \boldsymbol{\psi}_{n-1}}{2}\right). \tag{47}$$

4.2 Nonlinear Solver

On the fault, the slip-rate Eq. (46) and the state variable evolution equation Eq. (47) are discretized implicitly. Therefore, we must solve a nonlinear algebraic problem for slip velocity and the state variable. To formulate the nonlinear algebraic problem we consider collocated grid points on the sides of the fault. The dynamics of the the displacement field is governed by

$$u^-_{n+1} = 2u^-_n - u^-_{n-1} + \frac{\Delta t^2}{\widehat{\rho}^-} a^-_n + \frac{\Delta t^2}{\widehat{\rho}^- \gamma_1 h_q} \mathbf{J}|\mathbf{q}|\sigma_0 \frac{f(|V_n|, \psi_n))}{|V_n|} V_n, \tag{48}$$

$$u^+_{n+1} = 2u^+_n - u^+_{n-1} + \frac{\Delta t^2}{\widehat{\rho}^+} a^+_n - \frac{\Delta t^2}{\widehat{\rho}^+ \gamma_1 h_q} \mathbf{J}|\mathbf{q}|\sigma_0 \frac{f(|V_n|, \psi_n))}{|V_n|} V_n, \tag{49}$$

where

$$a^\pm_n = \widehat{\mathcal{D}}^{\mu^\pm} \mathbf{u}^\pm_n + \widehat{\mathbf{F}}^\pm_N \pm \frac{\mathbf{J}_N|\mathbf{q}_N|}{\gamma_1 h_q} \mathbf{T}_{0N},$$

is evaluated on the fault, and $h^{(q)}_i = \gamma_i h_q$, $\gamma_i > 0$ are the quadrature weights given by the SBP operator, with $\gamma_1 = \gamma_N$. Note that the slip-rate V_n is unknown, and it depends on the unknown displacement fields u^-_{n+1} and u^+_{n+1}.

First, we solve for the absolute slip-rate $|V_n|$. Combining Eq. (48) and Eq. (49) we have

$$|V_n| \left(\left(\frac{J_N|\mathbf{q}_N|}{2\gamma_1 \widehat{\rho}^-} + \frac{J_N|\mathbf{q}_N|}{2\gamma_1 \widehat{\rho}^+} \right) \frac{\Delta t}{h_q} \sigma_0 f(|V_n|, \psi_n) - |\Phi_n| + |V_n| \right) = 0, \tag{50}$$

where

$$\Phi_n = \frac{[\![u]\!]_n - [\![u]\!]_{n-1}}{\Delta t} + \frac{\Delta t}{2} \left(\frac{1}{\widehat{\rho}^+} a^+_n - \frac{1}{\widehat{\rho}^-} a^-_n \right). \tag{51}$$

Therefore we must have $|V_n| = 0$ or

$$\left(\frac{J_N|\mathbf{q}_N|}{2\gamma_1 \widehat{\rho}^-} + \frac{J_N|\mathbf{q}_N|}{2\gamma_1 \widehat{\rho}^+} \right) \frac{\Delta t}{h_q} \sigma_0 f(|V_n|, \psi_n) = |\Phi_n| - |V_n|. \tag{52}$$

Considering $|V_n| > 0$, we obtain the update equation Eq. (52) for the absolute slip-rate when fault is slipping.

It can be shown that with $\sigma_0 \geq 0$, for all $f(V,\psi)$ with $f(0,\psi) = 0$ and $\partial f(V,\psi)/\partial V > 0$ the nonlinear algebraic problem (52) for the absolute slip-rate $|V_n|$ has a unique solution. At each time step, the solution for the absolute slip-rate is in the closed interval $[0, |\Phi_n|]$. In particular, $|\Phi_n|$ defined in (51), approximates the frictionless, $\sigma_0 f(|V_n|, \psi_n) = 0$, slip-rate which is damped when friction is present, $\sigma_0 f(|V_n|, \psi_n) > 0$. Note also that if the fault is not slipping then the slip-rate vanishes identically, $|V_n| = 0$.

We solve (52) for $|V_n|$ using a bounded nonlinear root-finding algorithm such as the Regula-Falsi method. Consequently, we update the displacements using (49) and (48). Then, we compute the state variable ψ_{n+1} from (47) using a nonlinear rootfinding algorithm, such as Newton-Raphson with the initial guess $\psi_{n+1}^0 = \psi_n$, with the superscript keeping track of the Newton-Raphson iteration. Note that since the state evolution laws satisfy $\partial g(V,\psi)/\partial\psi < 0$, see (27)–(28), the Newton-Raphson iteration, for updating the state variable ψ_{n+1}, from (47), is guaranteed to converge.

We will explain this procedure more clearly. We first solve the nonlinear algebraic problem (50) for the absolute velocity $|V_n| \geq 0$. When $|V_n| > 0$, we compute

$$\alpha_- = \frac{J_N|\mathbf{q}_N|}{\widehat{\rho}^-\gamma_1 h_q}\sigma_0\frac{f(|V_n|,\psi_n)}{|V_n|}, \quad \alpha_+ = \frac{J_N|\mathbf{q}_N|}{\widehat{\rho}^+\gamma_1 h_q}\sigma_0\frac{f(|V_n|,\psi_n)}{|V_n|}, \quad A = 1 + \frac{1}{2}(\alpha_- + \alpha_+)\Delta t,$$

and update displacements on the fault using

$$\begin{aligned} u_{n+1}^- = \frac{1}{A}\Bigg[&\left(1 + \frac{\Delta t}{2}\alpha_+\right)\left(2u_n^- - u_{n-1}^- + \frac{\Delta t^2}{\rho^-}a_n^- + \frac{\Delta t\alpha_-}{2}[\![u]\!]_{n-1}\right) \\ &+\frac{\Delta t\alpha_-}{2}\left(2u_n^+ - u_{n-1}^+ + \frac{\Delta t^2}{\rho^+}a_n^+ - \frac{\Delta t\alpha_+}{2}[\![u]\!]_{n-1}\right)\Bigg], \end{aligned} \tag{53}$$

$$\begin{aligned} u_{n+1}^+ = \frac{1}{A}\Bigg[&\left(\frac{\Delta t}{2}\alpha_+\right)\left(2u_n^- - u_{n-1}^- + \frac{\Delta t^2}{\rho^-}a_n^- + \frac{\Delta t\alpha_-}{2}[\![u]\!]_{n-1}\right) \\ &+\left(1 + \frac{\Delta t\alpha_-}{2}\right)\left(2u_n^+ - u_{n-1}^+ + \frac{\Delta t^2}{\rho^+}a_n^+ - \frac{\Delta t\alpha_+}{2}[\![u]\!]_{n-1}\right)\Bigg]. \end{aligned} \tag{54}$$

When $|V_n| = 0$, we take the limit

$$|V_n| \to 0 \iff \sigma_0\frac{f(|V_n|,\psi_n)}{|V_n|} \to \infty,$$

obtaining

$$u_{n+1}^- = u_n^- + u_n^+ - u_{n-1}^+ + \frac{\Delta t^2}{2\rho^-}a_n^- + \frac{\Delta t^2}{2\rho^+}a_n^+, \tag{55}$$

$$u_{n+1}^+ = u_n^- + u_n^+ - u_{n-1}^- + \frac{\Delta t^2}{2\rho^-}a_n^- + \frac{\Delta t^2}{2\rho^+}a_n^+. \tag{56}$$

Note that (55), (56) satisfy

$$V_n := \frac{[\![u]\!]_{n+1} - [\![u]\!]_{n-1}}{2\Delta t} = 0,$$

Algorithm 1 Update displacements and the state variable on the fault

1: *loop*: over the grid points on the fault surface
2: on each grid point solve for the slip-rate $|V_n|$ from (52) using Regula-Falsi with the initial guess $|V_n|^0 = |V_{n-1}|$
3: **if** $|V_n| > 0$ **then** fault is slipping
4: compute the coefficients α_+, α_-
5: update displacements on the grid point using (54), (53)
6: **if** $|V_n| = 0$ **then** slip-rate vanishes
7: update displacements on the grid point using (56), (55)
8: **if** friction law: rate-and-state **then**
9: Solve for state from (47) using Newton-Raphson with the initial guess $\psi_{n+1}^0 = \psi_n$.

exactly, for all n. The algorithm to update displacements and the state variable on the fault is summarized in Algorithm 1 below.

Algorithm 1 can also be adapted for other frictions laws, such as the slip-weakening friction laws for which the friction coefficient is a function of slip, $f = f(|[\![u]\!]_n|)$. In this case, the stick absolute slip-rate is $|V_n| = 0$, and the sliding absolute slip-rate can be obtained from (52), having

$$|V_n| = |\Phi_n| - \left(\frac{J_N|\mathbf{q}_N|}{2\gamma_1\widehat{\rho}^-} + \frac{J_N|\mathbf{q}_N|}{2\gamma_1\widehat{\rho}^+}\right)\frac{\Delta t}{h_q}\sigma_0 f\left(|[\![u]\!]_n|\right), \tag{57}$$

without solving a nonlinear equation. The coefficients $\alpha_\pm$ used in (54), (53) for updating displacements are

$$\alpha_- = \frac{J_N|\mathbf{q}_N|}{\rho^-\gamma_1 h_q}\sigma_0\frac{f\left(|[\![u]\!]_n|\right)}{|V_n|}, \quad \alpha_+ = \frac{J_N|\mathbf{q}_N|}{\rho^+\gamma_1 h_q}\sigma_0\frac{f\left(|[\![u]\!]_n|\right)}{|V_n|}, \quad A = 1 + \frac{1}{2}(\alpha_- + \alpha_+)\Delta t.$$

Remark 2. *For the slip-weakening friction law, the solution* (57) *might be negative,* $|V_n| \le 0$, *when* $\left(\frac{J_N|\mathbf{q}_N|}{2\gamma_1\widehat{\rho}^-} + \frac{J_N|\mathbf{q}_N|}{2\gamma_1\widehat{\rho}^+}\right)\frac{\Delta t}{h_q}\sigma_0 f\left(|[\![u]\!]_n|\right) \ge |\Phi_n|$. *This is contradictory, and can only correspond to the stick condition, with vanishing slip-rate,* $|V_n| = 0$. *The physical solution satisfying* (50) *for this situation must be* $|V_n| = 0$. *The rate-and-state friction law is self-consistent, and does not have this feature.*

4.3 Fully Discrete Stability

We will now prove numerical stability of the fully discrete approximations (44)–(45). Our primary objective is to derive a fully discrete energy equation analogous to the continuous energy equation (20) and the semi-discrete energy equation (41).

To do this, we introduce the fully discrete inner product

$$\left\langle \mathbf{u}, \mathbf{v} \right\rangle := \mathbf{u}^T\mathbf{v}, \tag{58}$$

and the discrete quantities

$$\mathcal{K}_n = \Big\langle \frac{\mathbf{u}_{n+1} - \mathbf{u}_n}{\Delta t}, \left(\widehat{\rho}\mathbf{H} - \frac{\Delta t^2}{4}\mathcal{A}\right) \frac{\mathbf{u}_{n+1} - \mathbf{u}_n}{\Delta t} \Big\rangle, \tag{59}$$

$$\mathcal{U}_n = \Big\langle \frac{\mathbf{u}_{n+1} + \mathbf{u}_n}{2}, \mathcal{A}\frac{\mathbf{u}_{n+1} + \mathbf{u}_n}{2} \Big\rangle + \frac{1}{2}\begin{pmatrix}\mathbf{D}_q\left(\mathbf{u}_{n+1} + \mathbf{u}_n\right)\\ \mathbf{D}_r\left(\mathbf{u}_{n+1} + \mathbf{u}_n\right)\end{pmatrix}^T \mathbf{S}^T \begin{pmatrix}\mathbf{HJ} & \mathbf{0}\\ \mathbf{0} & \mathbf{HJ}\end{pmatrix}\begin{pmatrix}\boldsymbol{\sigma}^0_{xz}\\ \boldsymbol{\sigma}^0_{yz}\end{pmatrix} + \mathbf{U}_0, \tag{60}$$

where $\mathcal{A}$ is defined in (37) and $\mathbf{U}_0$ defined in (39). Now define

$$\mathcal{E}_n = \mathcal{K}_n + \mathcal{U}_n. \tag{61}$$

From Duru et al. (2011), we know that for some positive number $\gamma_{\text{cfl}} > 0$, such that $\triangle t \le \gamma_{\text{cfl}} h/c_{\max}$, with $h = \min\left(h_q/\sqrt{\mathbf{q}_x^2 + \mathbf{q}_y^2}, h_r/\sqrt{\mathbf{r}_x^2 + \mathbf{r}_y^2}\right)$, $c_{\max} = \max\left(\mathbf{c}\right)$, the discrete quantity $\mathcal{K}_n$ defined in (59) is strictly positive. Thus $\mathcal{K}_n > 0$ and $\mathcal{U}_n > 0$, defined in (59)–(60), approximate the fully discrete kinetic and strain energies. Here $\gamma_{\text{cfl}} > 0$ is a CFL number, with $\mathbf{c}$ being the shear wave speed. The CFL number $\gamma_{\text{cfl}} > 0$ depends on the order of accuracy of the spatial operator and $\gamma_{\text{cfl}} = 0.7071$ for second order accurate spatial operator. For the fourth and sixth order of accuracy the values are $\gamma_{\text{cfl}} = 0.7071/\sqrt{1.4498}$, $\gamma_{\text{cfl}} = 0.7071/\sqrt{2.1579}$, respectively. We can now prove that there is a CFL number $\gamma_{\text{cfl}} > 0$, independent of the mesh size h, the time step, and the friction law, such that:

Theorem 4. *If $\triangle t \le \gamma_{\text{cfl}} h/c_{\max}$, with $h = \min\left(h_q/\sqrt{\mathbf{q}_x^2 + \mathbf{q}_y^2}, h_r/\sqrt{\mathbf{r}_x^2 + \mathbf{r}_y^2}\right)$, $c_{\max} = \max\left(\mathbf{c}\right)$, then the quantity $\mathcal{E}_n$ defined in (61) is a fully discrete energy. The sum of the energies, $\mathcal{E}_n^- + \mathcal{E}_n^+$, satisfies*

$$\frac{\left(\mathcal{E}_{n+1}^+ + \mathcal{E}_{n+1}^-\right) - \left(\mathcal{E}_n^+ + \mathcal{E}_n^-\right)}{\Delta t} = -\sum_{j=1}^{N_r} \sigma_0 |V_{nj}| f\left(|V_{n,j}|, \psi_{n,j}\right) J_{Nj} |\boldsymbol{q}_{Nj}| h_j^{(r)}. \tag{62}$$

Proof. We use the fully discrete energy method, that is, from the left we multiply the Eq. (44) with $\left[\left(\mathbf{u}_{n+1}^- - \mathbf{u}_{n-1}^-\right)/2\Delta t\right]^T \mathbf{H}$ and Eq. (45) with $\left[\left(\mathbf{u}_{n+1}^+ - \mathbf{u}_{n-1}^+\right)/2\Delta t\right]^T \mathbf{H}$, add the transpose of the products. Using the summation-by-parts properties Eqs. (30)–(32), and considering boundary contributions from the fault only (while ignoring other boundaries) gives

$$\frac{\mathcal{E}_{n+1}^- - \mathcal{E}_{n-1}^-}{\Delta t} = \sum_{j=1}^{N_r} V_{nj}^- \widehat{T}_{nj} J_{Nj} |\mathbf{q}_{Nj}| h_j^{(r)}, \quad \frac{\mathcal{E}_{n+1}^+ - \mathcal{E}_{n-1}^+}{\Delta t} = -\sum_{j=1}^{N_r} V_{nj}^+ \widehat{T}_{nj} J_{Nj} |\mathbf{q}_{Nj}| h_j^{(r)} \tag{63}$$

with

$$\widehat{T}_{nj} = \sigma_0 \frac{f\left(|V_{nj}|, \boldsymbol{\psi}_j\right)}{|V_{nj}|} V_{nj}, \quad V_{nj} = V_{nj}^+ - V_{nj}^-, \quad V_{nj}^\pm = \frac{u_{n+1j}^\pm - u_{n-1j}^\pm}{2\Delta t},$$

evaluated along the fault. Again, we have utilized the fact that $\left(\mathbf{U}_{0n+1} - \mathbf{U}_{0n-1}\right)/2\Delta t \equiv 0$. Adding the contributions from both sides of the fault completes the proof. □

The fully discrete energy equation (62) completely mimics the energy equation (20) and the semi-discrete energy estimate (41). Clearly, the fully discrete energy is dissipated by friction, $\left[\mathcal{E}_{n+1}^{+} + \mathcal{E}_{n+1}^{-}\right] \le \left[\mathcal{E}_{n}^{+} + \mathcal{E}_{n}^{-}\right]$. When the slip-rate vanishes, $V_{nj} = 0$, the energy is conserved. It is also of significant importance to note that Remark 1 is applicable to the fully discrete approximation (44)–(45).

The stability of the approximation of the state evolution (47) is embedded in the implicit numerical discretization. The guaranteed convergence of the Newton-Raphson iteration for updating the state variable from (47) is a further testament of this fact. It is particularly noteworthy that the explicit time step is independent of the friction law, and is determined by the wave propagation problem.

5 Numerical Experiments

In this section we present numerical experiments. We first verify the accuracy, stability and convergence properties of the method. Then, we present numerical simulations verifying the understressing theory of Zheng and Rice (1998), and incorporating fully dynamic earthquakes into a method for simulating earthquake sequences in a power-law viscoelastic solid (Allison and Dunham, 2018).

5.1 Accuracy and Convergence

To verify numerical accuracy, we simulate the interaction of waves with friction in a simple 1D problem for which a semi-analytical solution can be constructed using the method of characteristics. We consider a 1D domain $-1 \le x \le 1$, with a fault located at $x = 0$, discretized with N grid points and a uniform spatial step $h = 1/(N-1)$. For this experiment, the fault boundary, at $x = 0$, is governed by a nonlinear rate-dependent friction law, with the nonlinear friction coefficient

$$f(V) = a\,\mathrm{arcsinh}\left(\beta V\right), \tag{64}$$

with $a > 0$ and $\beta > 0$. This formulation is widely used in earthquake mechanics and other frictional sliding problems, and can be theoretically related to how sliding is accommodated by thermally activated defect motion at microscopic contacts bridging the frictional interface (Kozdon et al., 2012; Rice et al., 2001).

The shear wave speed is 1 km/s and the shear modulus is 1 GPa. Because we assume the material parameters and displacement are symmetric about the fault, we can reduce the computational domain to $0 \le x \le 1.$, where $a = 1$ MPa and $\beta = 100$ s/m. The boundary at $x = 1$ km is closed with an absorbing boundary condition, allowing incident waves to exit the domain rather than reflect, by setting the incoming characteristics to zero. This boundary condition can be expressed as

$$\mu\frac{\partial u}{\partial x} + Z\frac{\partial u}{\partial t} = 0, \quad Z = \rho c_s, \tag{65}$$

the discretization of which is derived in Duru et al. (2014).

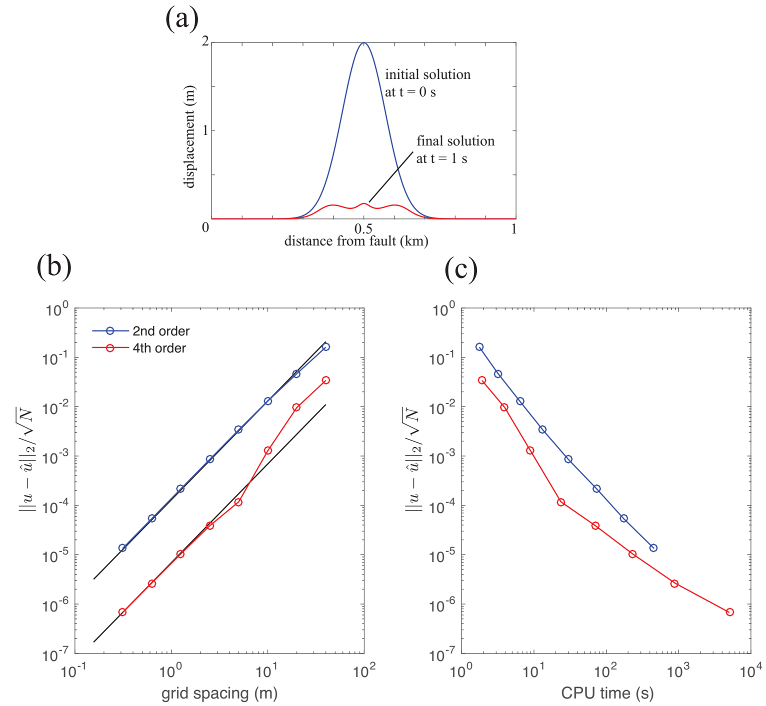

Figure 2: (a) Initial (blue) and final (red) displacement as a function of distance from the fault. (b) Convergence rates for SBP operators with 2nd (blue) and 4th (red) order spatial accuracy as a function of grid spacing, and expected slope of 2 (black). Note that because the temporal discretization is second order accurate, even the 4th order spatial accuracy converges with a slope of 2. (c) The relationship between CPU time and solution error.

We initiate the displacement field with a Gaussian perturbation in the center of the domain,

$$u_0(x) = 2e^{-(x-0.5)^2/0.01} \tag{66}$$

as shown in Figure 2a, and with the medium initially at rest. We run the simulation for 1 s, so that waves generated by the initial perturbation reach the fault boundary, reflect, and return the location of the initial perturbation. The final displacement field is also shown in Figure 2a. Both second and fourth order accurate spatial discretizations are tested. We compare the numerical solutions u with that of a semi-analytical solution $\hat{u}$ based on the method of characteristics. That is, we decompose the solutions into characteristics, plane shear waves, propagating to the right and left of the domain. The nonlinear frictional boundary condition leads to a nonlinear algebraic equation. Thus we have a closed form solution for the displacement field

$$\hat{u}(x,t) = \phi(x,t) + \int_0^{t-x/c_s} V(\tau)d\tau, \tag{67}$$

$$\phi(x,t) = \frac{1}{2}\left(u_0(x - c_s t) + u_0(x + c_s t)\right), \tag{68}$$

where the slip-rate V satisfies the nonlinear algebraic equation

$$\Phi(\tau) - ZV(\tau) - f\left(V(\tau)\right) = 0, \quad \Phi(\tau) = \mu \frac{\partial}{\partial x}\phi(x,\tau)\Big|_{x=0}. \tag{69}$$

Here, $\Phi(\tau)$ is the shear stress generated by the initial data, and propagated by the characteristic $\phi(x,t)$ to the fault boundary. The stress term $\Phi(\tau)$ loads the fault. We have chosen the initial condition $u_0(x)$ and frictional parameters, a, β, such that $\Phi(\tau)$ is sufficiently large to initiate slip. The fault stops slipping as soon as the characteristic wave field $\phi(x,t)$ leaves the domain.

This nonlinear problem (69) is solved for the slip-rate with a Newton-Raphson solver. To compute the result in terms of displacement (67), the slip-rate is integrated along the characteristics using the recursive adaptive Simpson quadrature. Note that a small amount of numerical error is introduced by the nonlinear solver and the numerical quadrature, which can be made arbitrarily small by choosing parameters such that the tolerance is very close the machine precision $\sim 10^{-16}$.

Figure 2b demonstrates that the numerical solutions converge to the exact (semi-analytical) solution (67) with second order accuracy for both cases. This is expected since the time discretization is second order accurate. However, the magnitude of the errors generated by the fourth order accurate spatial approximation is much smaller than the errors for the second order accurate case. In addition, Figure 2c demonstrates that the fourth order accurate scheme is more efficient, requiring less CPU time for a given error tolerance.

5.2 Transition in Rupture Style

Simulations of earthquakes produce two basic rupture modes, the self-healing slip pulse and the expanding crack. In the self-healing slip pulse mode, only the portion of the fault at the rupture front slips, and slip ceases behind the rupture front as the fault heals. In the expanding crack mode, slip begins at the rupture front, but the fault continues to slip everywhere within the rupture zone. This phenomenology is observed in shear ruptures in the laboratory (Lykotrafitis et al., 2006). Many lines of reasoning suggest that natural earthquakes occur in the self-healing rupture mode (Heaton, 1990). The goal of this numerical experiment is to simulate this transition in rupture style.

For uniform prestress conditions on faults governed by a strongly rate-weakening friction law, Eq. (24) and (26), the rupture mode is primarily determined by the background shear stress on the fault, τ^{b}. According to the understressing theory of Zheng and Rice (1998) for ruptures in elastic solids, there exists a critical background stress level, τ^{pulse}, below which ruptures cannot take the form of cracks. An additional, lower threshold below which slip pulses are not self-sustaining is also observed in numerical simulations. Thus, self-sustaining slip pulses occur within a narrow range of τ^{b} around τ^{pulse} (Zheng and Rice, 1998; Noda et al., 2009). For the steady state friction law (26) with our chosen parameters (Table 1), the critical background stress τ^{pulse}, as defined by Zheng and Rice (1998), is $\tau^{\mathrm{pulse}} = 0.2429\sigma_0$ ($= 30.6059$ MPa for $\sigma_0 = 126$ MPa). This transition is observed in our simulation results, shown in Figure 3. For these simulations, we used a domain of 20 km by 20 km, grid spacing of 100 m, and a time step of 7.2 ms. All boundary conditions are absorbing boundaries, as in Eq. 65.

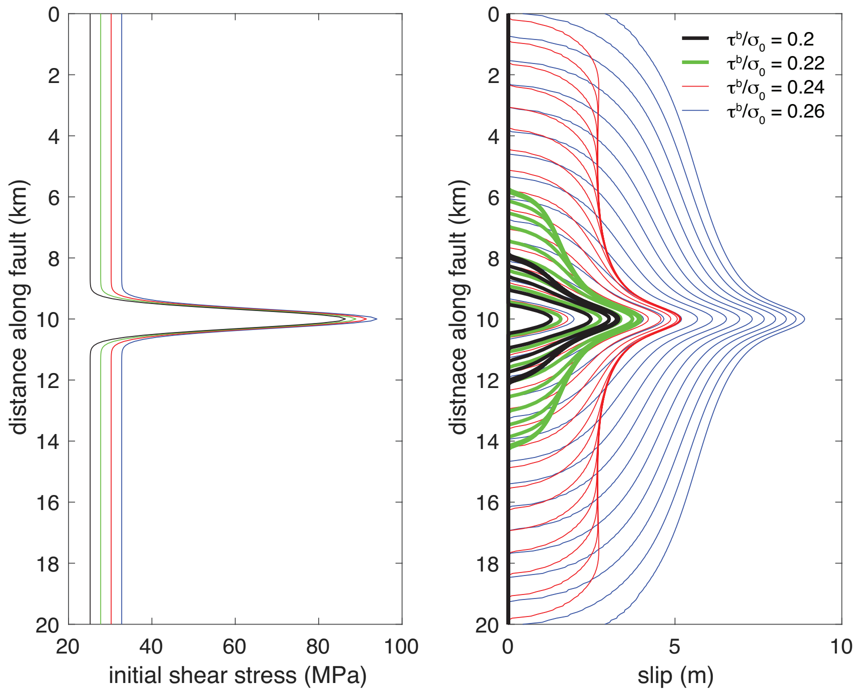

Figure 3: (a) Initial shear stress is $\tau^b + 2\tau_{pulse}\exp(-(y-10)^2/0.18)$. (b) Slip contoured every 0.25 s for the initial shear stress profiles shown in (a). Self-sustaining ruptures occur for $\tau^b/\sigma_0 \geq 0.23$, and the transition between slip pulse and crack-like ruptures occurs when $\tau^b/\sigma_0 = 0.26$.

5.3 Earthquake Sequences in a Viscoelastic Solid

Fully dynamic simulations of single earthquakes, such as those presented in the previous section, capture the physics of dynamic rupture and wave propagation; however, earthquakes are artificially initiated by overstressing a small portion of the fault (e.g., Figure 3a). A more realistic approach is to simulate the entire earthquake cycle, during which gradually imposed tectonic loading during the interseismic phase builds up a stress concentration that spontaneously nucleates an earthquake which is fully consistent with the friction law, material response, and loading. Earthquake sequence simulation methods frequently use the quasi-dynamic approximation, in which computational cost is reduced by neglecting wave-mediated stress transfer (e.g., Rice, 1993; Ben-Zion and Rice, 1995; Kato, 2002; Ziv and Cochard, 2006; Erickson and Dunham, 2014; Allison and Dunham, 2018). Though the quasi-dynamic approximation is accurate for low slip-rates, when employed during earthquakes it produces slower slip-rates and rupture speeds than the fully dynamic problem would produce (Thomas et al., 2014). Some numerical methods are able to simulate elastodynamics through all phases of the earthquake cycle (e.g., Lapusta et al., 2000; Lapusta and Liu, 2009; Barbot et al., 2012). Others employ a quasi-static or quasi-dynamic method during the interseismic period and switch to a fully dynamic method when the earthquake nucleates (e.g., Okubo, 1989; Shibazaki and Matsu'ura, 1992; Kaneko et al., 2011). Here, we take

Table 1: Parameters used to investigate the transition from crack-like to pulse-like ruptures.

parameter	symbol	value
initial state variable	ψ	0.4367
direct effect parameter	a	0.016
state evolution effect parameter	b	0.02
reference friction coefficient for steady sliding	f_0	0.7
reference velocity	V_0	10^{-6} m s^{-1}
fully weakened friction coefficient	f_w	0.13 m s^{-1}
weakening velocity	V_w	0.17 m s^{-1}
state evolution distance	d_c	0.2572 m
shear wave speed	c_s	3.464 km s^{-1}
density of rock	ρ	2.7 g cm^{-3}

the latter approach, integrating the inertial solver developed in this paper into the quasi-dynamic sequence method developed for linear elasticity in Erickson and Dunham (2014) and extended to viscoelasticity in Allison and Dunham (2018). During the coseismic period, the viscoelastic off-fault material is effectively elastic, so we are able to use the method developed in this work without modification. A description of the viscoelastic governing equations, using identical notation, can be found in Allison and Dunham (2018).

We perform an example simulation using the model geometry and material properties shown in Figure 4 and Table 2, using a 500 km by 500 km domain to avoid reflections from the boundaries. Because the material properties are symmetric about the fault, we are able to solve for only the $x \geq 0$ portion of the domain, reducing the computational expense. The fault is governed by rate-and-state friction, for which we use the regularized form (22) and the aging law for state evolution (23). We set total normal stress using the lithostatic gradient, and use hydrostatic pore pressure to determine effective normal stress (e.g., Sibson, 1974). The rheological parameters for the crust (wet feldspar) are from Rybacki et al. (2006) and those for the mantle (wet olivine) are from Hirth and Kohlstedt (2003).

During the interseismic period, the rheology of the viscoelastic off-fault material is

$$\sigma_{xz} = \mu \left(\frac{\partial u}{\partial x} - \gamma^V_{xz} \right), \quad \sigma_{yz} = \mu \left(\frac{\partial u}{\partial y} - \gamma^V_{yz} \right), \tag{70}$$

$$\dot{\gamma}^V_{xz} = \eta^{-1}_{\text{eff}} \sigma_{xz}, \quad \dot{\gamma}^V_{yz} = \eta^{-1}_{\text{eff}} \sigma_{yz}, \tag{71}$$

$$\eta^{-1}_{\text{eff}} = A e^{-Q/RT} \bar{\tau}^{n-1}, \quad \bar{\tau} = \sqrt{\sigma^2_{xz} + \sigma^2_{yz}}, \tag{72}$$

where u is the displacement in the z direction, γ^V_{ij} are the (engineering) viscous strains, η_{eff} is the effective viscosity, and T is the temperature. The overdot indicates a time derivative. In the flow law, the effective viscosity is a function of the rate coefficient A, the activation energy Q, the gas constant R, the stress exponent n, and the deviatoric stress $\bar{\tau}$.

During the coseismic period, the governing equations are those described in Section 2.2. We use a traction-free condition at the top of the domain, and enforce outgoing characteristics

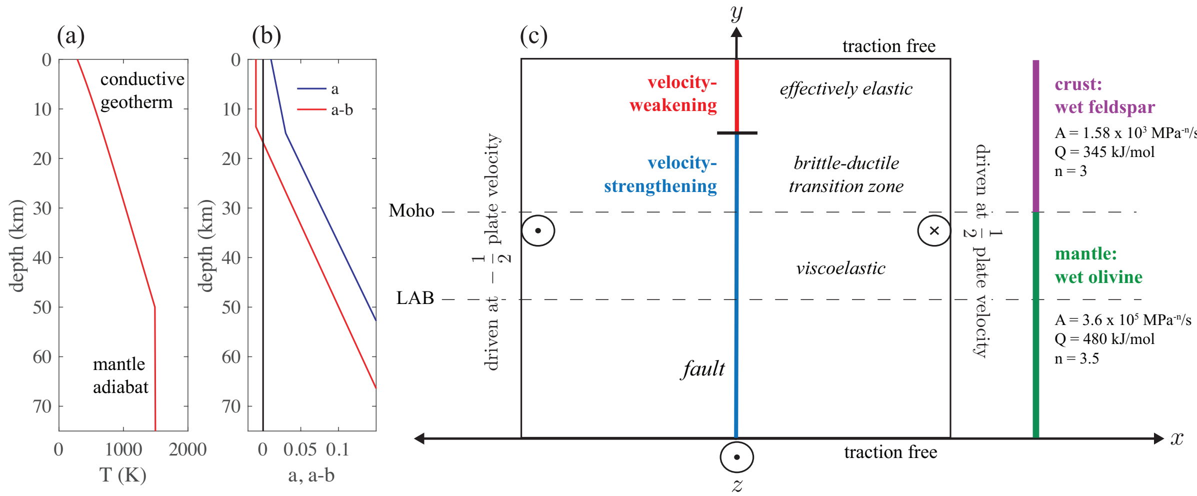

Figure 4: Model set-up for earthquake sequence simulation in a viscoelastic solid with fully dynamic coseismic phase: (a) geotherm, (b) rate-and-state friction parameters, (c) model diagram and rheological parameters. The boundary conditions shown are used for the quasi-dynamic periods.

Table 2: Parameters used in viscoelastic earthquake cycle simulations.

parameter	symbol	value
reference friction coefficient for steady sliding	f_0	0.6
reference velocity	V_0	10^{-6} m s^{-1}
state evolution distance	d_c	0.02 m
density of rock	ρ	2.7 g cm^{-3}
shear modulus	μ	32.4 GPa
tectonic plate velocity	V_p	10^{-9} m/s

for the bottom and right boundaries

$$\sigma_{zx}(x, L_y, t) = 0 \tag{73}$$

$$\sigma_{zy}(x, 0, t) = \rho c_s u_t, \tag{74}$$

$$\sigma_{zx}(L_x, y, t) = -\rho c_s u_t, \tag{75}$$

which allows the waves generated by the earthquake to exit the domain.

To ensure accuracy, it is necessary to resolve the critical length scale for unstable elastic sliding between elastic half-spaces with rate-and-state friction (e.g. Ruina, 1983; Rice, 1983; Rice et al., 2001)

$$h^* = \frac{\mu d_c}{\sigma_n(b-a)}, \tag{76}$$

and the length scale of cohesive-zone size (Palmer, 1973; Dieterich, 1992; Day et al., 2005; Ampuero and Rubin, 2008)

$$L_b = \frac{\mu d_c}{\sigma_n b}. \tag{77}$$

For the parameters used here, (77) is the more stringent criteria, and we use a grid spacing of $L_b/8$ (as small as 2.3 m) near the velocity-weakening region of the fault, with aggressive grid stretching away from this region (as large as 15 km) to accommodate the large domain.

The results for two cycles are shown in Figure 5, in which the interseismic period lasts 320 years and the coseismic period lasts 20 s. A quasi-dynamic simulation with otherwise identical parameters is shown in Figure 6 for comparison. The interseismic period, which is quasidynamic in both simulations, is quite similar. In the purely quasi-dynamic simulation, the recurrence interval is slightly shorter, 300 years, and the slow slip event is slightly smaller. The coseismic period, however, differs substantially. In the fully dynamic case, the upgoing rupture tip propagates at the shear wave speed, and the reflection off of the Earth's surface is clearly visible. In contrast, in the quasidynamic case, the rupture propagates at a much slower speed, and the uppermost 3 km of the fault accelerates to earthquake slip velocities before the upgoing rupture tip actually propagates to this region. Additionally, in the quasi-dynamic case the effect of the rupture reaching Earth's surface is instantly communicated everywhere in the domain, rather than being propagated at the shear wave speed.

We switch between quasi-dynamic and fully dynamic solvers based on the nondimensional ratio $R = \eta V/\tau_{qs}$, where the numerator is the radiation damping term and the denominator is the quasi-static shear stress, and $\eta = 0.5\mu/c_s$ is the radiation damping parameter. Quasi-static shear stress is computed as T^+ in Equation 5. For the fully dynamic solver, this is equivalent to the shear stress on the fault, τ, but for the quasi-dynamic solver $\tau = \tau_{qs} - \eta V$. When inertia is negligible, the magnitude of the radiation damping term is very small and $\max(R) \ll 1$. The effect of different threshold values of $\max(R)$ for switching at the beginning and end of the coseismic period is shown in Figure 7. We find that the overall system behavior is relatively insensitive to the switching criteria selected, provided that R is sufficiently small. Because the choice of more stringent criteria substantially increases the computational cost, we use $\max(R) = 10^{-3}$ to control switching both into and out of the fully dynamic solvers.

The primary advantage of the second-order formulation developed in this paper is that it can be integrated into a quasidynamic earthquake sequence method. An additional advantage is that, relative to the first-order form on an unstaggered grid, the second-order form reduces spurious high frequency oscillations. Figure 8 compares these formulations using initial conditions from Figure 5c with two different grid spacings: a mesh that marginally resolves the rupture with grid spacing equal to $L_b/2.5$, and a more refined mesh with grid spacing equal to $L_b/5$. The first-order formulation results were produced using the code FDMAP (Dunham et al., 2011; Kozdon et al., 2012, 2013), with 4th and 6th order accurate SBP operators. The formulation developed in this paper is shown only with 4th order operators. (These orders of accuracy correspond to those of the interior difference operators.)

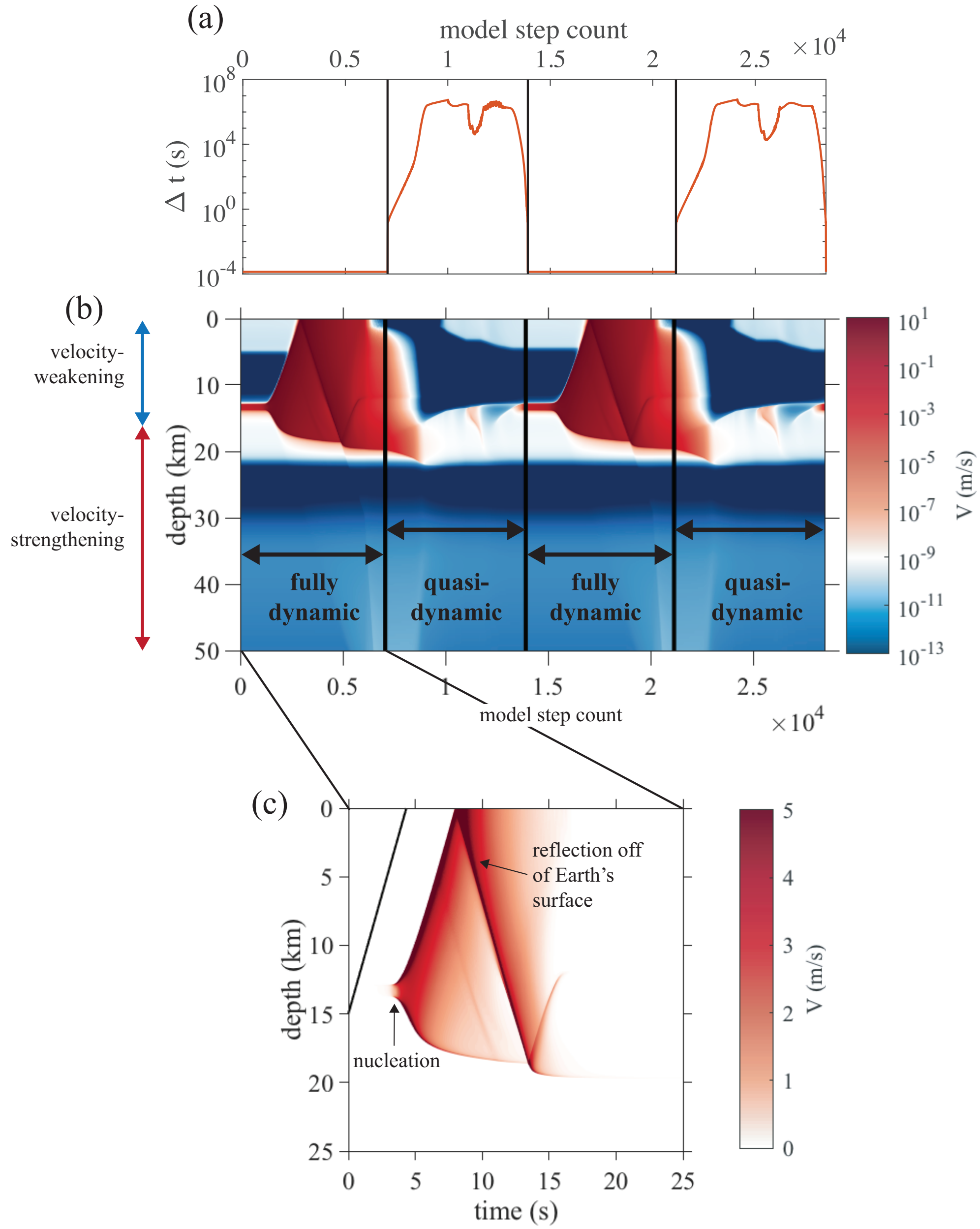

Figure 5: Earthquake sequence simulation in a viscoelastic solid, with fully dynamic coseismic phase. (a) Time step is constant during the coseismic periods, when the fully dynamic wave equation is solved, and adaptively chosen during the interseismic period when the quasi-dynamic approximation is used. (b) slip-rate for two earthquake cycles, plotted as a function of step count not time, and showing only a subset of steps. The fully dynamic phase lasts 20 s, and the quasi-dynamic phase lasts 320 years. (c) Close up of a single earthquake, plotted as a function of time. The black line shows the shear wave speed.

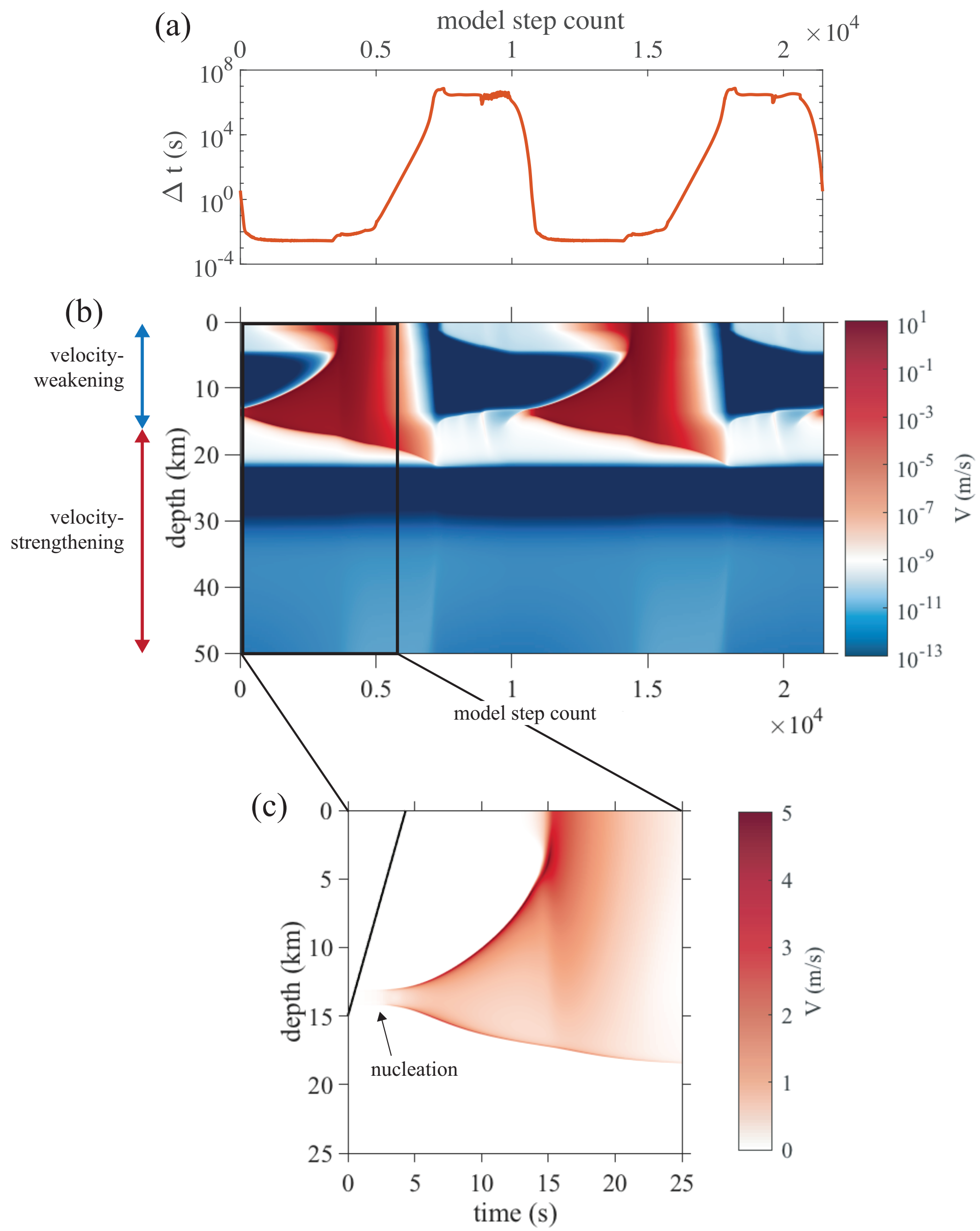

Figure 6: Same as Figure 5, but with quasi-dynamic solver used for the coseismic phase.

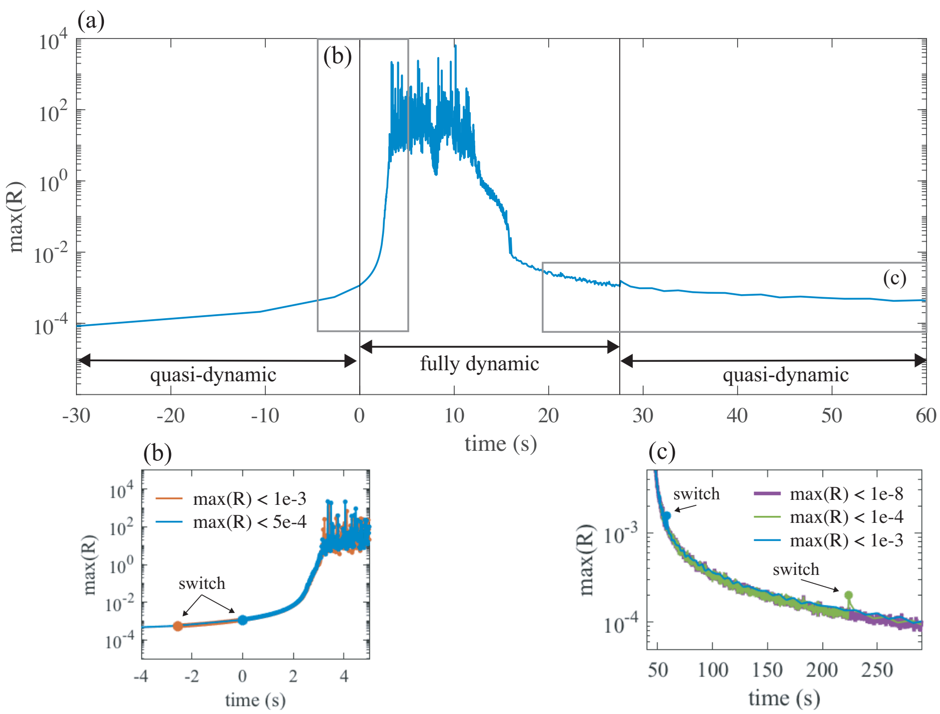

Figure 7: (a) max(R) as a function of time since the onset of the earthquake for the simulation plotted in Figure 5. Grey boxes indicate the portion illustrated in (b) and (c). (b) Comparison between switching criteria at the start of the earthquake. The filled circles indicate the time of the switch from the quasi-dynamic solver to the fully dynamic solver. (c) Comparison between switching criteria at the end of the earthquake. The filled circles indicate the time of the switch from the fully dynamic solver to the quasi-dynamic solver. Note that the blue lines in (a), (b), and (c) all correspond to the same simulation.

1st order wave eq.
2nd order wave eq.

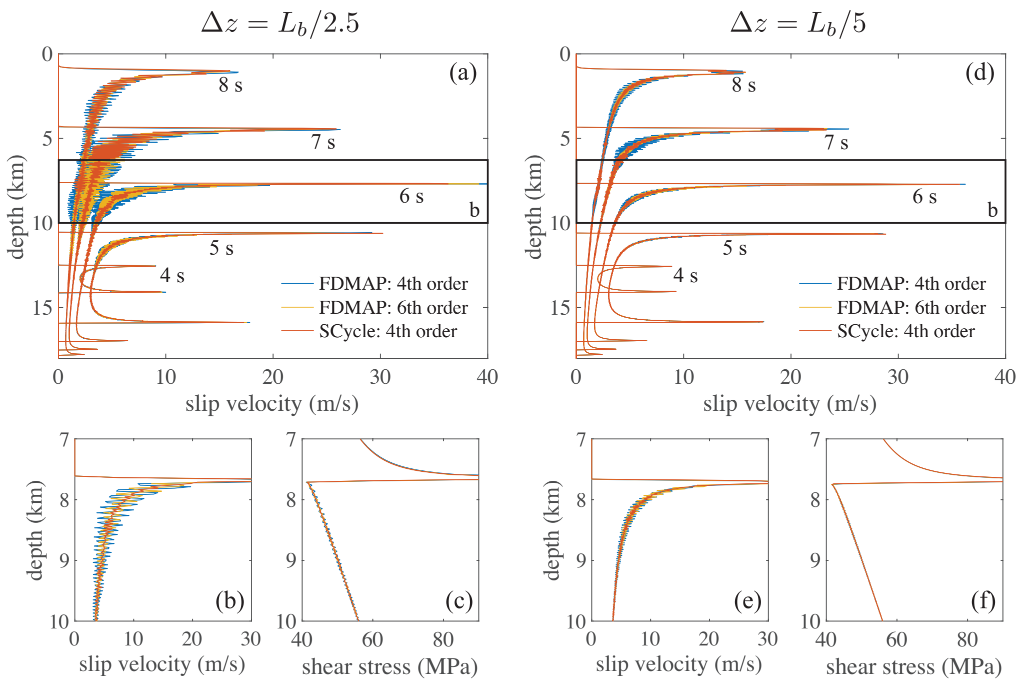

Figure 8: Comparison of a fully dynamic rupture at selected times for the first-order formulation, using FDMAP with 4th (blue) and 6th (yellow) order accurate SBP operators, and the second-order formulation, using 4th order accurate SBP operators (red). Marginally resolved: (a) Slip velocity contours at selected times. (b) and (c) Close up of slip velocity and shear stress at the rupture front at 6 s. More highly resolved: (d) Slip velocity contours at selected times. (e) and (f) Close up of slip velocity and shear stress at the rupture front at 6 s.

6 Summary and Outlook

This paper presents a provably stable and accurate method for the simulation of fully dynamic earthquake ruptures in antiplane strain. The elastic wave equation is written in second-order form, and the discretization is performed using SBP finite differences. The main result of the paper is the derivation of a stable treatment for a nonlinear fault interface condition (rate-and-state friction) which is enforced weakly. As examples illustrate, the method can be applied to study single dynamic rupture events as well as earthquake cycles. Future efforts could extend this approach to the 2D plane strain and 3D problems.

Acknowledgements

The project has received funding from the European Union's Horizon 2020 research and innovation program under grant agreement No 671698.

K.D. developed and wrote up the numerics. M.R. integrated the method into a pre-existing quasidynamic earthquake cycle code, with support from K.L.A. K.L.A. performed and wrote up the numerical experiments. K.D., K.L.A., and E.M.D. provided critical feedback and helped shape the research, analysis, and manuscript.

References

Allison, K. L., and E. M. Dunham (2018), Earthquake cycle simulations with rate-and-state friction and power-law viscoelasticity, doi:10.1016/j.tecto.2017.10.021.

Ampuero, J.-P., and A. M. Rubin (2008), Earthquake nucleation on rate and state faults - Aging and slip laws, *Journal of Geophysical Research*, *113*(B1), doi:10.1029/2007JB005082.

Andrews, D. J., and S. Ma (2016), Validating a dynamic earthquake model to produce realistic ground motion, *Bulletin of the Seismological Society of America*, *106*(2), 665–672, doi:10.1785/0120150251.

Appelö, D., and N. A. Petersson (2009), A stable finite difference method for the elastic wave equation on complex geometries with free surfaces, *Communications in Computational Physics*, *5*(1), 84–107.

Barbot, S., N. Lapusta, and J.-P. Avouac (2012), Under the hood of the earthquake machine: Toward predictive modeling of the seismic cycle, *Science*, *336*(May), 707–710, doi:10.1126/science.1218796.

Beeler, N. M., and T. E. Tullis (2003), Constitutive relationships for fault strength due to flash heating, in *SCEC Annual Meeting Proceedings and Abstracts, vol. XIII*, p. 66, South. Calif. Earthquake Center, Los Angeles.

Beeler, N. M., T. E. Tullis, and D. L. Goldsby (2008), Constitutive relationships and physical basis of fault strength due to flash heating, *Journal of Geophysical Research*, *113*(B1), B01,401, doi:10.1029/2007JB004988.

Ben-Zion, Y., and J. R. Rice (1995), Slip patterns and earthquake populations along different classes of faults in elastic solids, *Journal of Geophysical Research: Solid Earth*, *100*(B7), 12,959–12,983, doi:10.1029/94JB03037.

Birkhoff, G., and G.-C. Rota (1989), *Ordinary differential equations*, 4th ed. ed., 399 pp., Wiley, New York, doi:10.1137/1.9780898719222.

Dahlquist, G. (2010), Numerical methods for ordinary differential equations, lecture notes.

Day, S. M. (1982), Three-dimensional simulation of spontaneous rupture: the effect of nonuniform prestress, *Bulletin of the Seismological Society of America*, *72*(6), 1881–1902.

Day, S. M., L. A. Dalguer, N. Lapusta, and Y. Liu (2005), Comparison of finite difference and boundary integral solutions to three-dimensional spontaneous rupture, *Journal of Geophysical Research*, *110*(12), 1–23, doi:10.1029/2005JB003813.

Dieterich, J. H. (1979), Modeling of rock friction 1. Experimental results and constitutive equations, *Journal of Geophysical Research: Solid Earth*, *84*(B5), 2161–2168, doi:10.1029/JB084iB05p02161.

Dieterich, J. H. (1992), Earthquake nucleation on faults with rate-and state-dependent strength, *Tectonophysics*, *211*(1), 115–134, doi:10.1016/0040-1951(92)90055-B.

Douilly, R., H. Aochi, E. Calais, and A. M. Freed (2015), Three-dimensional dynamic rupture simulations across interacting faults: The Mw7.0, 2010, Haiti earthquake, *Journal of Geophysical Research: Solid Earth*, *120*(2), 1108–1128, doi:10.1002/2014JB011595.

Dunham, E. M., D. Belanger, L. Cong, and J. E. Kozdon (2011), Earthquake ruptures with strongly rate-weakening friction and off-fault plasticity, part 1: Planar faults, *Bulletin of the Seismological Society of America*, *101*(5), 2296–2307.

Duru, K., and K. Virta (2014), Stable and high order accurate difference methods for the elastic wave equation in discontinuous media, *Journal of Computational Physics*, *279*, 37–62, doi:10.1016/j.jcp.2014.08.046.

Duru, K., K. Mattsson, and G. Kreiss (2011), Stable and conservative time propagators for second order hyperbolic systems, *Tech. rep.*, Division of Scientific Computing, Departmet of Information Technology, Uppsala University.

Duru, K., G. Kreiss, and K. Mattsson (2014), Stable and high-order accurate boundary treatments for the elastic wave equation on second-order form, *SIAM Journal on Scientific Computing*, *36*(6), doi:10.1137/130947210.

Erickson, B. A., and S. M. Day (2016), Bimaterial effects in an earthquake cycle model using rate-and-state friction, *Journal of Geophysical Research: Solid Earth*, *121*(4), 2480–2506, doi:10.1002/2015JB012470.

Erickson, B. A., and E. M. Dunham (2014), An efficient numerical method for earthquake cycles in heterogeneous media: Alternating subbasin and surface-rupturing events on faults crossing a sedimentary basin, *Journal of Geophysical Research: Solid Earth*, *119*(4), 3290–3316, doi:10.1002/2013JB010614.

Heaton, T. H. (1990), Evidence for and implications of self-healing pulses of slip in earthquake rupture, *Physics of the Earth and Planetary Interiors*, *64*(1), 1–20, doi:10.1016/0031-9201(90)90002-F.

Hirth, G., and D. Kohlstedt (2003), Rheology of the upper mantle and the mantle wedge: A view from the experimentalists, *Geophysical Monograph Series*, *138*, 83–105, doi:10.1029/138GM06.

Kaneko, Y., J. P. Ampuero, and N. Lapusta (2011), Spectral-element simulations of long-term fault slip: Effect of low-rigidity layers on earthquake-cycle dynamics, *Journal of Geophysical Research: Solid Earth*, *116*(10), doi:10.1029/2011JB008395.

Kato, N. (2002), Seismic cycle on a strike-slip fault with rate- and state-dependent strength in an elastic layer overlying a viscoelastic half-space, *Earth, Planets and Space*, *54*(11), 1077–1083, doi:10.1186/BF03353305.

Kostrov, V. V. (1974), Seismic moment and energy of earthquakes, and seismic flow of rock, *Earth Physics*, *1*, 23–40.

Kozdon, J. E., E. M. Dunham, and J. Nordstrom (2012), Interaction of waves with frictional interfaces using summation-by-parts difference operators: Weak enforcement of nonlinear boundary conditions, *Journal of Scientific Computing*, *50*(2), 341–367, doi:10.1007/s10915-011-9485-3.

Kozdon, J. E., E. M. Dunham, and J. Nordstrom (2013), Simulation of dynamic earthquake ruptures in complex geometries using high-order finite difference methods, *Journal of Scientific Computing*, *55*(1), 92–124, doi:10.1007/s10915-012-9624-5.

Kreiss, H.-O., and J. Oliger (1972), Comparison of accurate methods for the integration of hyperbolic equations, *Tellus*, *24*(3), 199–215, doi:10.1111/j.2153-3490.1972.tb01547.x.

Kreiss, H.-O., N. A. Petersson, and J. Yström (2002), Difference approximations for the second order wave equation, *SIAM Journal on Numerical Analysis*, *40*(5), 1940–1967, doi:10.1137/S0036142901397435.

Lapusta, N., and Y. Liu (2009), Three-dimensional boundary integral modeling of spontaneous earthquake sequences and aseismic slip, *Journal of Geophysical Research: Solid Earth*, *114*(9), B09,303, doi:10.1029/2008JB005934.

Lapusta, N., J. R. Rice, Y. Ben-Zion, and G. Zheng (2000), Elastodynamic analysis for slow tectonic loading with spontaneous rupture episodes on faults with rate- and state-dependent friction, *Journal of Geophysical Research: Solid Earth*, *105*(B10), 23,765–23,789, doi:10.1029/2000JB900250.

Lykotrafitis, G., A. J. Rosakis, and G. Ravichandran (2006), Self-healing pulse-like shear ruptures in the laboratory, *Science*, *313*(September), 1765–1769.

Marfurt, K. J. (1984), Accuracy of finite difference and finite element modeling of the scalar and elastic wave equations, doi:10.1190/1.1441689.

Marone, C. (1998), Laboratory-derived friction laws and their application to seismic faulting, *Annual Review of Earth and Planetary Sciences*, *26*(1), 643–696, doi:10.1146/annurev.earth.26.1.643.

Mattsson, K. (2011), Summation by parts operators for finite difference approximations of second-derivatives with variable coefficients, *Journal of Scientific Computing*, *51*(3), 650–682, doi:10.1007/s10915-011-9525-z.

Noda, H., and N. Lapusta (2010), Three-dimensional earthquake sequence simulations with evolving temperature and pore pressure due to shear heating: Effect of heterogeneous hydraulic diffusivity, *Journal of Geophysical Research: Solid Earth*, *115*(B12314), doi:10.1029/2010JB007780.

Noda, H., E. M. Dunham, and J. R. Rice (2009), Earthquake ruptures with thermal weakening and the operation of major faults at low overall stress levels, *Journal of Geophysical Research*, *114*, doi:10.1029/2008JB006143.

Okubo, P. G. (1989), Dynamic rupture modeling with laboratory-derived constitutive relations, *Journal of Geophysical Research*, *94*(B9), 12,321–12,335, doi:10.1029/JB094iB09p12321.

Palmer, A. R. J. (1973), The growth of slip surfaces in the progressive failure of over-consolidated clay, *Proceedings of the Royal Society A: Mathematical, Physical and Engineering Sciences*, *332*(1591), 527–548.

Rice, J. R. (1983), Constitutive relations for fault slip and earthquake instabilities, *Pure and Applied Geophysics PAGEOPH*, *121*(3), 443–475, doi:10.1007/BF02590151.

Rice, J. R. (1993), Spatiotemporal complexity of slip on a fault, *Journal of Geophysical Research*, *98*(B6), 9885–9907, doi:10.1029/93JB00191.

Rice, J. R. (1999), Flash heating at asperity contacts and rate-dependent friction, in *Eos Transactions, AGU Fall Meeting Supplement 80(46)*, p. F681l.

Rice, J. R. (2006), Heating and weakening of faults during earthquake slip, *Journal of Geophysical Research: Solid Earth*, *111*(5), doi:10.1029/2005JB004006.

Rice, J. R., and A. L. Ruina (1983), Stability of steady frictional slipping, *Journal of Applied Mechanics*, *50*(2), 343–349, doi:10.1115/1.3167042.

Rice, J. R., N. Lapusta, and K. Ranjith (2001), Rate and state dependent friction and the stability of sliding between elastically deformable solids, *Journal of the Mechanics and Physics of Solids*, *49*, 1865–1898, doi:10.1016/S0022-5096(01)00042-4.

Rudnicki, J. W., and L. B. Freund (1981), On energy radiation from seismic sources, *Bull. Seism. Soc. Am.*, *71*(3), 583–595.

Ruina, A. (1983), Slip instability and state variable friction laws, *Journal of Geophysical Research: Solid Earth*, *88*(B12), 10,359–10,370, doi:10.1029/JB088iB12p10359.

Rybacki, E., M. Gottschalk, R. Wirth, and G. Dresen (2006), Influence of water fugacity and activation volume on the flow properties of fine-grained anorthite aggregates, *Journal of Geophysical Research: Solid Earth*, *111*(B3), n/a–n/a, doi:10.1029/2005JB003663.

Saenger, E. H., N. Gold, and S. A. Shapiro (2000), Modeling the propagation of elastic waves using a modified finite-difference grid, *Wave Motion*, *31*(1), 77–92, doi:10.1016/S0165-2125(99)00023-2.

Scholz, C. H. (1998), Earthquakes and friction laws, *Nature*, *391*(6662), 37–42, doi:10.1038/34097.

Segall, P., and A. M. Bradley (2012), The Role of Thermal Pressurization and Dilatancy in Controlling the Rate of Fault Slip, *Journal of Applied Mechanics*, *79*(3), 031,013, doi:10.1115/1.4005896.

Shi, Z., and S. M. Day (2013), Rupture dynamics and ground motion from 3-D rough-fault simulations, *Journal of Geophysical Research: Solid Earth*, *118*(3), 1122–1141, doi:10.1002/jgrb.50094.

Shibazaki, B., and M. Matsu'ura (1992), Spontaneous processes for nucleation, dynamic propagation, and stop of earthquake rupture, *Geophysical Research Letters*, *19*(12), 1189–1192, doi:10.1029/92GL01072.

Sibson, R. H. (1974), Frictional constraints on thrust, wrench and normal faults, *Nature*, *249*, 542–544, doi:10.1038/249542a0.

Sjögreen, B., and N. A. Petersson (2011), A fourth order accurate finite difference scheme for the elastic wave equation in second order formulation, *Journal of Scientific Computing*, *52*(1), 17–48, doi:10.1007/s10915-011-9531-1.

Thomas, M. Y., N. Lapusta, H. Noda, and J. P. Avouac (2014), Quasi-dynamic versus fully dynamic simulations of earthquakes and aseismic slip with and without enhanced coseismic weakening, *Journal of Geophysical Research: Solid Earth*, *119*(3), 1986–2004, doi:10.1002/2013JB010615.

Virieux, J. (1986), P-SV wave propagation in heterogeneous media: Velocity-stress finite-difference method, *Geophysics*, *51*(4), 889–901, doi:10.1190/1.1442147.

Zheng, G., and J. R. Rice (1998), Conditions under which velocity-weakening friction allows a self-healing versus a cracklike mode of rupture, *Bulletin of the Seismological Society of America*, *88*(6), 1466–1483.

Zingg, D. W. (2000), Comparison of high-accuracy finite-difference methods for linear wave propagation, *SIAM Journal on Scientific Computing*, *22*(2), 476–502, doi:10.1137/S1064827599350320.

Ziv, A., and A. Cochard (2006), Quasi-dynamic modeling of seismicity on a fault with depth-variable rate- and state-dependent friction, *Journal of Geophysical Research: Solid Earth*, *111*(8), B08,310, doi:10.1029/2005JB004189.